Budget Analysis of a Tropical Cyclone Simulated in an Axisymmetric Numerical Model

Yoshio Kurihara

Geophysical Fluid Dynamics Laboratory/NOAA, Princeton University, Princeton, N. J. 08540

(Manuscript received 29 March 1974)

ABSTRACT

A tropical cyclone simulated in an axisymmetric numerical model is analyzed in detail from various aspects in order to deepen the understanding of the basic mechanisms of its evolution. Namely, the budget equations of temperature, moisture, relative angular momentum, vorticity, radial-vertical circulation, and kinetic energy are investigated for the different stages of the development of a tropical cyclone. The spatial distributions of each term in the budget equations are shown and their role in the following processes are discussed.

In the pre-deepening stage of a large weak vortex in a conditionally unstable atmosphere, a solenoidal field is formed as a result of a delicate heat budget which depends on the static stability and the moisture content. The baroclinicity field thus established drives the system into a deepening stage. A positive feedback process builds up a warm moist core, accelerates the radial-vertical circulation, and intensifies the moist convection. A net outflow of mass from the central region and a resultant drop of central surface pressure take place during this period. The relative angular momentum of the inner column as a whole increases through convergence of relative angular momentum. In terms of relative vorticity, intensification and shrinking of the vortex is due to the combined effects of advection, horizontal convergence and twisting. At the end of the deepening stage, conditional instability in the central region is neutralized. The moment due to Coriolis force acting on the intensified azimuthal flow counterbalances the baroclinicity vector, so that the acceleration of radial-vertical flow ceases. Concentration of relative angular momentum and vorticity in the central region also levels off. In the budget of these quantities, the role of both vertical and lateral stress becomes important. In the troposphere, except the upper part and the boundary layer, the gradient wind relationship is established between the pressure field and the azimuthal flow. In the mature stage, the status in the inner region is quasi-stationary while that of the outer area keeps changing slowly. The importance of evaporation at the central area for the maintenance of an intense tropical cyclone is demonstrated in an additional experiment.

1. Introduction

The purpose of this paper is to present the results of budget analyses of a simulated axisymmetric tropical cyclone in order to deepen the understanding of the mechanism of its evolution.

The formation of tropical cyclones has been investigated for many years through theoretical works and also through analysis of observed meteorological data. In the early 1960's, this research was enhanced by a new tool, a numerical simulation model. The modeling of a tropical cyclone requires that the basic mechanisms of development and maintenance be incorporated into a model in an appropriate manner. The numerical experiments produce valuable data, by the analyses of which the important mechanism may be confirmed or clarified and even new findings may be made.

The capability of the numerical simulation approach to explain the basic mechanism of a tropical cyclone has been demonstrated by many works (e.g., Ooyama, 1969a, b; Yamasaki, 1968a, b; Rosenthal, 1969; Sundqvist, 1970; Anthes et al., 1971a; Kurihara and Tuleya, 1974). However, various problems have remained unanswered. Some examples are the budget of angular momentum, the detailed energetics including moisture budget, the quantitative analysis of the development of radial-vertical circulation, etc. These subjects are treated in the present paper.

The numerical model used in this study is the symmetric analogue of the three-dimensional model which has been constructed at the Geophysical Fluid Dynamics Laboratory, NOAA. The structure of a tropical cyclone in the latter model has been described (Kurihara and Tuleya, 1974) and the budgets of angular momentum and energy have been analyzed (Tuleya and Kurihara, 1975). The results show that, at least in the model, the asymmetric field does not play a major role in the dynamics of a tropical cyclone. This is in contrast to the crucial role of the large-scale eddies in the general circulation. Thus, the basic mechanism of a tropical cyclone seems to be well explained by using an axisymmetric model, the analysis of which is simpler than that of an asymmetric model. The structural similarity between the asymmetric storm and the symmetric model storm at the mature stage was also noticed by Anthes et al. (1971b).

2. Description of the model

a. Basic equations

The numerical model used in the present study is the axisymmetric analogue of the three-dimensional, 11-level primitive equation model which is described in detail by Kurihara and Tuleya (1974, hereafter referred to as A).

The model uses a constant f-plane ($f = 5 \times 10^{-5}$ s^{-1}) approximation, and is formulated in the sigma-coordinate system originally proposed by Phillips (1957). Putting the center of the axisymmetric vortex at the origin of a cylindrical σ-coordinate system, the basic equations are written as follows:

Equation of motion

$$\frac{\partial}{\partial t}(p_* u) = -D(u) + \left(f + \frac{v}{x}\right)p_* v - p_* \frac{\partial \phi_p}{\partial x} + {}_\mathrm{H}F_u + {}_\mathrm{V}F_u, \quad (2.1)$$

$$\frac{\partial}{\partial t}(p_* v) = -D(v) - \left(f + \frac{v}{x}\right)p_* u + {}_\mathrm{H}F_v + {}_\mathrm{V}F_v, \quad (2.2)$$

where t is time, x the radius, u the radial (outward) component of horizontal wind, v the azimuthal (counterclockwise) component of horizontal wind, and p_* the surface pressure. The operator D denotes the divergence

$$D(\ ) = \frac{\partial(\ )p_* ux}{x \partial x} + \frac{\partial(\ )p_* \dot\sigma}{\partial \sigma}, \quad (2.3)$$

where $\sigma = p/p_*$, p is the pressure, and $\dot\sigma = d\sigma/dt$. The pressure gradient force is obtained from the slope of the geopotential ϕ_p of an isobaric surface. The frictional forces due to horizontal and vertical diffusion of momentum are represented by the last two terms in (2.1) and (2.2).

Tendency equation

$$\frac{\partial p_*}{\partial t} = -D(1) = -\int_0^1 \frac{\partial p_* ux}{x \partial x} d\sigma, \quad (2.4)$$

where the boundary conditions, $\dot\sigma = 0$ at $\sigma = 0$ and 1, are implied.

Vertical σ-velocity

$$\sigma = \frac{1}{p_*}\left(-\sigma \frac{\partial p_*}{\partial t} - \int_0^\sigma \frac{\partial p_* ux}{x \partial x} d\sigma\right) \quad (2.5)$$

Vertical p-velocity

$$\omega = \frac{dp}{dt} = -p_* \sigma\left(-\frac{\dot\sigma}{\sigma} + \frac{\partial \dot\sigma}{\partial \sigma} + \frac{\partial ux}{x \partial x}\right) \quad (2.6)$$

Hydrostatic relation

$$\frac{\partial \phi}{\partial \ln \sigma} = -RT, \quad (2.7)$$

or

$$\phi - RT = \frac{\partial \phi \sigma}{\partial \sigma}, \quad (2.8)$$

TABLE 1. The σ-levels and their approximate heights.

Level k	σ	height (m)
0.5	0.00000000	
1.0	0.03060333	23,637
1.5	0.08318847	17,270
2.0	0.12000000	14,940
2.5	0.17310091	12,616
3.0	0.21500000	11,242
3.5	0.26704077	9,847
4.0	0.33500000	8,328
4.5	0.42025419	6,738
5.0	0.50000000	5,478
5.5	0.59487807	4,168
6.0	0.66500000	3,311
6.5	0.74338763	2,424
7.0	0.80000000	1,843
7.5	0.86092366	1,258
8.0	0.89500000	926
8.5	0.93042512	575
9.0	0.95000000	435
9.5	0.96998671	260
10.0	0.97700000	196
10.5	0.98406400	132
11.0	0.99200000	68
11.5	1.00000000	0

FIG. 1. Vertical division of the model atmosphere into 11 layers.

where ϕ is the geopotential of a constant σ-surface, T the temperature, and R the gas constant.

Thermodynamic equation

$$\frac{\partial}{\partial t}(p_* T) = -D(T) + \frac{R}{c_p}\frac{T\omega}{\sigma} + {}_HF_T + {}_VF_T + \text{QCON}, \quad (2.9)$$

where c_p is the specific heat of air at constant pressure. The last three terms are the effects of horizontal diffusion, of vertical diffusion, and of the condensation-convection processes, respectively. The radiation effect is ignored in the present modeling.

Equation for mixing ratio of water vapor

$$\frac{\partial}{\partial t}(p_* r) = -D(r) + {}_HF_r + {}_VF_r + \text{RCON}, \quad (2.10)$$

where r is the mixing ratio of water vapor and the meaning of the last three terms is similar to that of the corresponding terms in (2.9).

b. Grid system

The model atmosphere is divided into 11 layers. The position of the integer k level in each layer and that of half-integer level which defines an interface between the layers are listed in Table 1. [See Kurihara (1968) for the definition of half-levels.] As shown in Fig. 1, the variables u, v, T, r and ω are defined at integer k levels whereas ϕ and $\dot{\sigma}$ are defined at half-integer levels. The geopotential ϕ_p of an isobaric surface is obtained from the height of the nearest sigma surface by applying (2.7).
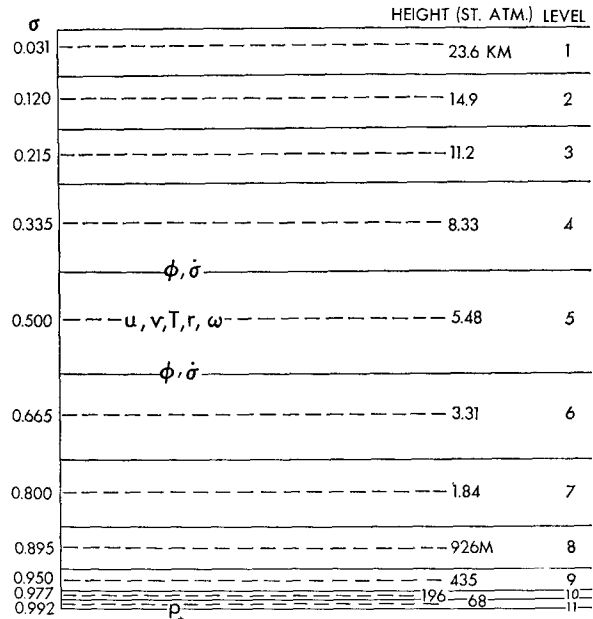
A free-slip, insulated lateral boundary encloses the present model in a domain of 2000 km radius. A domain of such a big size is chosen in order to make the influence of the lateral boundary on the storm structure near the center fairly small (see Rosenthal, 1971). It should be noted that the integration of the present model is not intended to obtain a steady state in the whole closed domain. In fact, the status at the mature stage of the storm is quasi-stationary only in the center area and it is not steady in the outer area. This is clearly shown in Section 9 where the analysis of angular momentum is presented. At any rate, constraints of both closed domain and axisymmetry have to be eliminated for a simulation of a

TABLE 2. Grid position and the width of the ring. The x coordinate of grid and width (Δx) of the rings are listed.

Grid index	x (km)	Δx (km)	Grid index	x (km)	Δx (km)
1	10	20	19	470.5	55
2	30	20	20	530	64
3	50	20	21	598.5	73
4	70	20	22	676	82
5	90	20	23	762	90
6	110	20	24	854.5	95
7	130	20	25	951	98
8	150	20	26	1050	100
9	170	20	27	1150	100
10	190	20	28	1250	100
11	210.5	21	29	1350	100
12	232	22	30	1450	100
13	255	24	31	1550	100
14	280.5	26	32	1650	100
15	307.5	29	33	1750	100
16	339	34	34	1850	100
17	376	40	35	1950	100
18	419.5	47			

realistic outer area which may or may not be quasi-steady.

The whole domain is divided into 35 concentric rings, each having a radially non-staggered grid at the center. The distance of grids from the coordinate center and the width of rings are shown in Table 2.

The space finite-difference scheme appropriate to the above defined grid system is essentially the same as the box method applied for the asymmetric version of the model, and the reader is referred to paper A.

c. Lateral boundary conditions

At the outer lateral boundary, both the grid-scale and subgrid-scale normal flux of any quantity are assumed to vanish. The normal component of the pressure gradient force is obtained so that the tangential wind at the wall satisfies the gradient wind balance.

At the coordinate center, the radial flux of any quantity vanishes and the radial gradient of pressure is set to be zero.

d. Subgrid-scale processes

Details of parameterization scheme for subgrid-scale processes are described in A. The principles only are mentioned below.

1) SUBGRID-SCALE HORIZONTAL DIFFUSION

The scheme of nonlinear viscosity (Smagorinsky, 1963) is formally applied to the present model. The horizontal diffusion coefficient for momentum, heat and moisture depends on the pure deformation, which is evaluated from the tension, i.e., $-2\partial u/\partial x$, and the shearing rate of strain, i.e., $-x\partial(v/x)/\partial x$. The diffusion coefficient at the mature stage of the cyclone becomes about 5×10^7 cm^2 s^{-1} in most regions of the domain. It exceeds 10^8 cm^2 s^{-1} in the troposphere at radial distances between about 40 and 150 km and also below the tropopause at distances between 600 and 1200 km.

2) SUBGRID-SCALE VERTICAL DIFFUSION

In the present model, the exchange of momentum, heat and water vapor at the sea surface is estimated by using a Monin-Obukhov type formulation (e.g., Delsol et al., 1971). The sea surface temperature is fixed to 302 K throughout the integration period.

Vertical diffusion in the free atmosphere is treated by parameterizing the effect of free convection and that of mechanical turbulence separately. The former is formulated in a dry convective adjustment scheme, while the latter is evaluated by using the vertical diffusion coefficient. The coefficient is computed by an extended application of the formula originally developed for the surface layer by Ellison (1957). It is Richardson-number dependent and different for

momentum and for heat. [See Eqs. (3.23)–(3.29) in A.] The coefficient for momentum at the mature stage of the cyclone is computed to be 10^4 cm^2 s^{-1} in most parts of the planetary boundary layer; greater than 10^5 cm^2 s^{-1} in the boundary layer within 200 km radius; and generally 10^2–10^3 cm^2 s^{-1} above the boundary layer. In the boundary layer the coefficient for heat is slightly smaller than that for momentum, but above the boundary layer it is smaller by two orders of magnitude.

3) MOIST CONVECTIVE ADJUSTMENT

The ensemble effect of moist convection is approximated through the adjustment of the temperature and moisture fields (Kurihara, 1973). It is assumed that free moist convection takes place when a hypothetical cloud element can become buoyant for a small vertical displacement in a given environment. Then the environmental field is stabilized so that the new adjusted state is neutral or just critical for free moist convection. The stabilization is achieved by the liberation of latent energy and the upward transport of heat and moisture.

Transport of momentum by cumulus convection is not incorporated in the present model.

3. Initial conditions and time integration

The initial condition is specified to establish a large weak vortex in gradient wind balance in a conditionally unstable model atmosphere. Specifically, it is computed as follows:

(i) $T(x,\sigma)$ is obtained from the integration of an approximate thermal wind relation (derived for a certain wind profile):

$$\frac{\partial T}{\partial x} = \begin{cases} -\dfrac{\sigma}{0.9}\dfrac{f}{R}V(x), & \text{for } \sigma < 0.9 \\ 0, & \text{for } 0.9 \leqslant \sigma \leqslant \sigma_{11} \end{cases} \qquad (3.1)$$

where $V(x)$ is chosen so that it becomes negligibly small near the lateral boundary:

$$V(x) = \hat{V}\frac{2(x/\hat{x})}{1+(x/\hat{x})^3}. \qquad (3.2)$$

In the present experiment, $\hat{V} = 12$ m s^{-1} and $\hat{x} = 200$ km are assumed. For the integration, T at $x = 5000$ km [i.e., $T(5000,\sigma)$] is as specified in Table 3.

(ii) $p_*(x)$ is computed from

$$\frac{\partial p_*}{\partial x} = \rho f V(x). \qquad (3.3)$$

In this study, $p_*(5000) = 1010$ mb and $\rho = 1.56\times10^{-3}$ gm cm^{-3} are used.

(iii) Wind component v is computed for each grid point by the finite-difference analogue of the gradient wind relation

$$\frac{v^2}{x} + fv = \frac{\partial \phi_p}{\partial x}, \tag{3.4}$$

while u is zero everywhere.

(iv) Mixing ratio is computed from the relative humidity specified in Table 3.

The maximum v of the initial vortex is 8.64 m s^{-1} at level 11 and at $x = 190$ km. At level 11, v is larger than 5 m s^{-1} for the range from $x = 90$ to 420 km. The wind decreases almost linearly with σ and it is less than 1 m s^{-1} at levels 1 and 2. Beyond $x = 1100$ km, v is less than 1 m s^{-1} at all levels. The initial p_* is 1009.77 mb at $x = 1950$ km and decreases gradually to 1005.63 mb at $x = 10$ km.

The initial T is almost horizontally uniform. The difference in T between the center and the outer boundary is largest at level 8 with a value of 0.9 K. The mixing ratio is about 22 g kg^{-1} at level 11 and about 16 g kg^{-1} at level 8. The equivalent potential temperature at levels 11, 5 and 2 are approximately 355, 327 and 350 K, respectively. This indicates a conditionally unstable state.

Starting from the above initial state, the time integration with the Euler backward marching scheme is carried out for a period of 240 h. The time step is 45 s, and any oscillations with a period of several minutes are thus suppressed. The damping property of the Euler backward scheme is apparently favorable rather than harmful for obtaining meaningful numerical results from a model in which the pressure field

TABLE 3. Temperature $T(5000,\sigma)$ and relative humidity used for setting the initial conditions.

Level	σ	$T(5000,\sigma)$ (K)	Relative humidity (percent)
1	0.031	218.7	0
2	0.120	200.3	0
3	0.215	223.9	5
4	0.335	247.4	10
5	0.500	267.8	30
6	0.665	281.1	60
7	0.800	289.9	75
8	0.895	294.9	85
9	0.950	297.7	90
10	0.977	299.1	95
11	0.992	299.8	98

tends to be disturbed continuously by strong condensation processes.

4. Classification of evolution stages

An hourly plot of central surface pressure is given in Fig. 2. The minimum pressure observed in the model is 930.7 mb at Hour 115.

Based on the examination of the time variation of various quantities including the surface pressure, the life cycle of the model tropical cyclone is divided into three evolution stages: Pre-deepening (Hours 0–60), Deepening (Hours 60–92) and Mature (Hours 92–240). For analysis purposes, a few sub-periods are further defined in each stage as indicated in Fig. 2. They are P1(Hours 1–20), P2(20–40), P3(40–60), D1(61–72), D2(72–83), M1(97–118), M2(170–186) and M3(224–239). The mean status for each period is defined by taking the average of the hourly analyses in that period. Such an averaging process will smooth out the
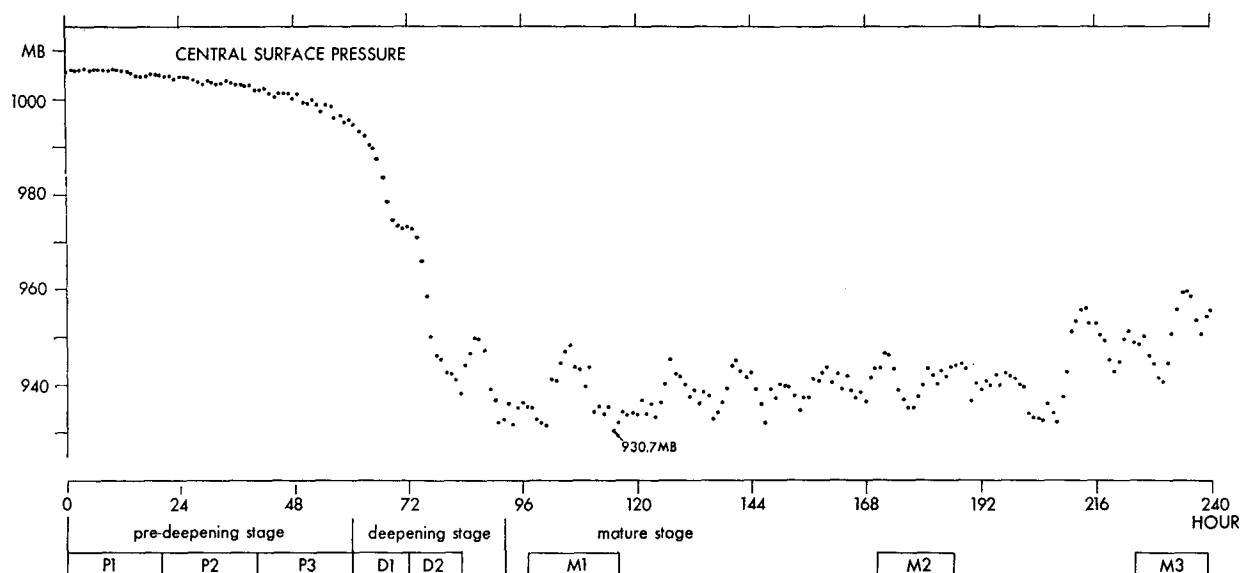

FIG. 2. Hourly plot of central surface pressure. Classification of evolution stages is shown at the bottom of the figure.
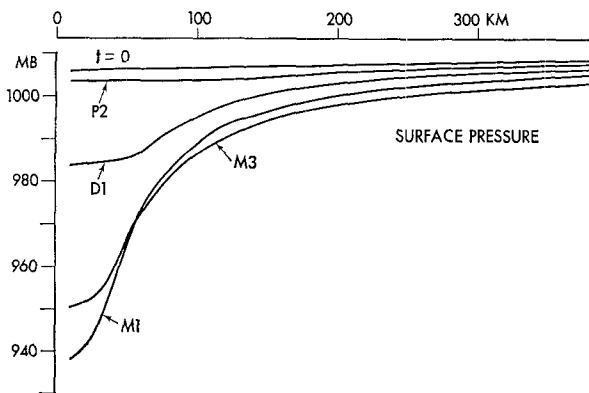
Fig. 3. Radial distribution of surface pressure at $t=0$
for periods P2, D1, M1 and M3.

components which oscillate with a period shorter than the averaging time.

It should be noted that there is no wave stage in the life cycle of the simulated tropical cyclone because of the axisymmetric constraint imposed on the present numerical model.

5. Variation of surface pressure and wind

The radial distributions of the surface pressure at the initial time and the periods P2, D1, M1 and M3 are shown in Fig. 3. The pressure drop during the period D1 through M1 near the center is more than 40 mb. Thus the surface pressure gradient increases sharply. At the later period of the mature stage, i.e., M3, the central pressure becomes slightly shallower as compared to the pressure at M1. However, the general tendency is that the pressure within 1250 km

radius still keeps decreasing throughout the mature stage. The area mean surface pressure inside 500 km radius changes from 1002.3 mb at M1 to 1000.3 at M3, and that inside 1000 km decreases from 1006.8 mb at M1 to 1005.8 mb at M3. Of course, the surface pressure beyond 1250 km increases since the total mass equivalent to the mean surface pressure 1009.4 mb is exactly conserved during the whole integration period.

The maximum surface wind or, more precisely, the maximum wind at the level $\sigma=0.992$, is plotted for every hour in Fig. 4. Winds of hurricane force are reached at Hour 65. An oscillation with a period of about 12 h is in evidence.

In Fig. 4, the time variation of the area mean precipitation and evaporation are also shown. It is seen that the mean precipitation is larger than the mean evaporation, implying the decrease of mean precipitable water during the integration period. The mean precipitation in the present experiment is very small because the rainfall is concentrated in a small inner region and the rest of the domain has little rainfall. For example, in the period M1, the precipitation per hour at 50 km radius is 50 mm and the mean value within 500 km radius is 0.86 mm.

Fig. 5 shows the radial distribution of wind speed at $\sigma=0.992$ at different periods. The position of maximum wind moves inward starting from 190 km at $t=0$ until it nears 50 km at M1. During the period from M1 to M3, the maximum speed drops while the speed beyond 80 km increases slightly. This increase will be discussed in Section 9 from the viewpoint of the budget of relative angular momentum.

The surface wind has no radial component at $t=0$. Within several hours after the start of the time inte-
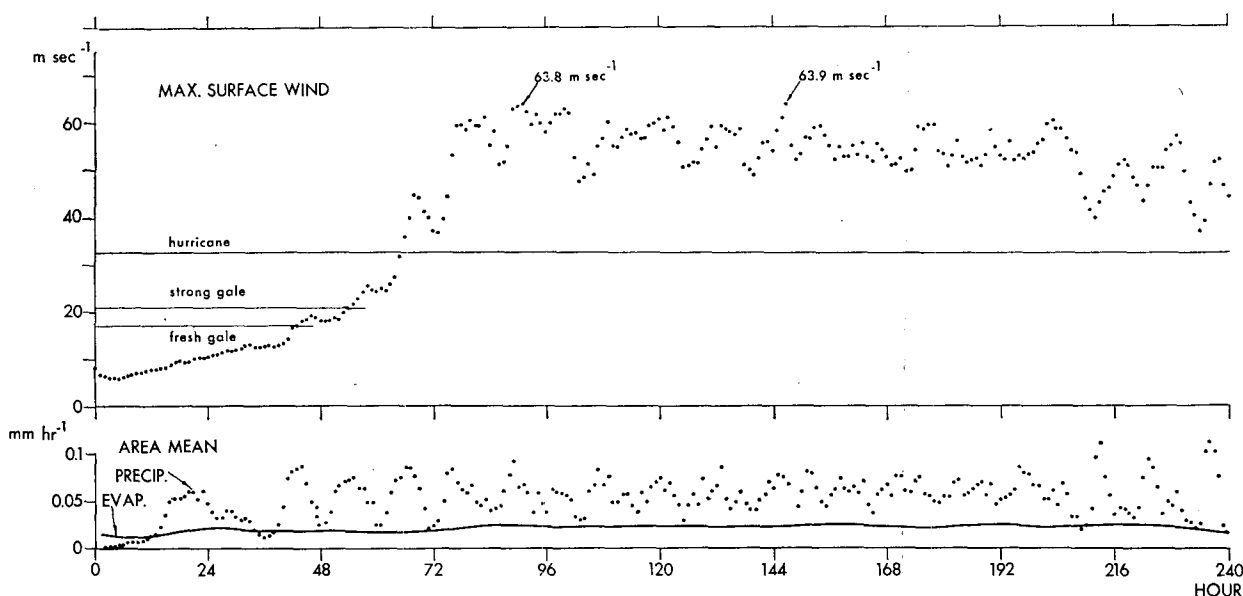

Fig. 4. Time variation of maximum wind at level 11, area mean precipitation, and area mean evaporation.
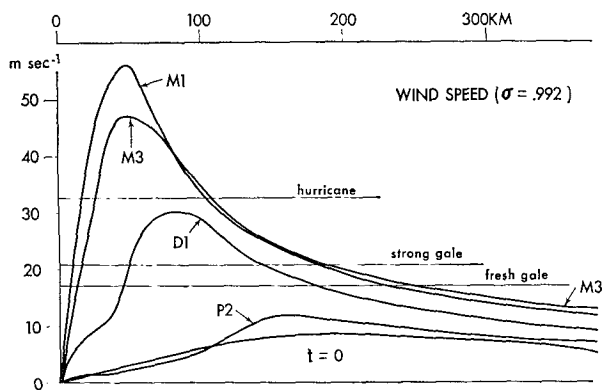
FIG. 5. Radial distribution of wind speed at level 11
at $t=0$ for periods P2, D1, M1 and M3.

gration, the inflow in the lower layers is established as a result of the boundary layer processes. Fig. 6 shows the variation of the surface wind vector with radius at different time levels. The inflow angle exceeds 40° at about 60 km from the center in the mature stage and gradually decreases outward.

6. Major structural changes of the vortex

In the course of time integration, the symmetric vortex undergoes various structural changes. The most noticeable ones are 1) neutralization of the conditional instability in the inner core region or the development of a warm moist core, 2) intensification of the azimuthal flow, 3) development of a radial-vertical circulation, and 4) shrinking of the vortex.

In this section, the features of the above-mentioned interrelated changes are briefly described. The causes or the processes of these structural changes will be discussed in the later sections.

Fig. 7 shows vertical profiles of the equivalent potential temperature at 0, 40, 80 and 120 km radii at Hours 60, 75, 105 and 180. The dotted curves in the figure indicate the initial distribution. At Hour 60, i.e., at the beginning of the deepening stage, a change in the equivalent potential temperature is noticeable, but the stratification remains conditionally unstable. At Hour 75, when rapid deepening is taking place, the inner part, especially at around 40 km radius, is approaching a moist neutral stage. The curve for Hour 105 shows that the conditional instability at 0 and 40 km radius is almost neutralized when the storm reaches the mature stage. Also note the increase of surface values. As time goes on further, the neutralized area slowly expands.

Next, the velocity field is examined. The vertical cross sections of the azimuthal component of the horizontal wind for periods P2, D1 and M1 are shown in Fig. 8. The intensity of cyclonic flow keeps increasing and the position of maximum v moves inward by the end of the deepening stage. After period M1,

the cyclonic flow in the outer lower region still increases slowly, but the maximum speed in the inner region drops a little. In Fig. 8, the position of maximum azimuthal flow in the horizontal and vertical is indicated by the dash-dotted line. It is seen from the figure that the maximum azimuthal speed at all levels is found at almost the same distance from the center except near the surface where the position of maximum speed is nearer the center. The azimuthal flow near the center varies very little with height. Elsewhere, the speed is the largest at a pressure level about 50 mb above the surface. Thus, the azimuthal component of wind increases with height in the boundary layer and decreases with height in the free atmosphere.

Another noticeable feature in the time variation of azimuthal motion is the development of anticyclonic flow in a certain region. Such a flow is observed, in period P1, at level 2 beyond 150 km radius. In period P2, the area of anticyclonic motion expands down to levels 3 and 4, then the area shifts outward. As shown in Fig. 8, the flow is anticyclonic, in period M1, in the upper layers at a distance beyond about 300 km. The area of negative v extends to the lateral boundary. A weak anticyclonic flow also appears at the top level in the inner region.

Fig. 9 shows the radial-vertical distribution of the radial component of the wind. Radial flow is established in a short period after the initial state of no radial motion. In periods P2 through D1, the general pattern of radial flow is outflow at levels 2 and 3 and
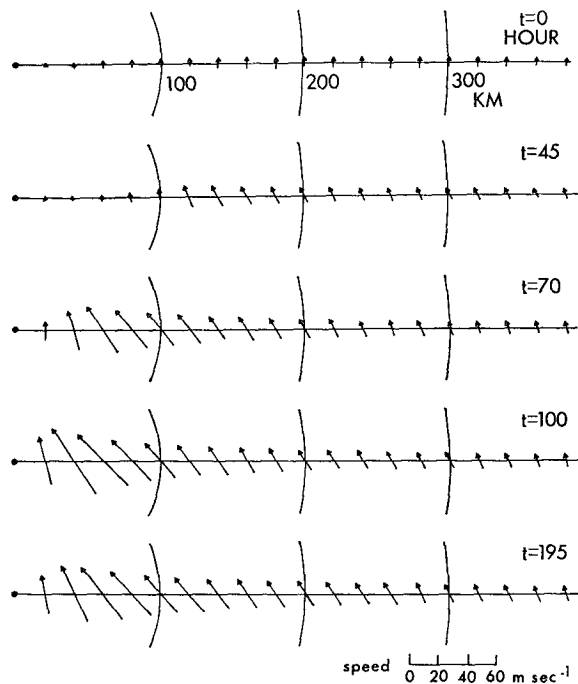

FIG. 6. Radial distribution of wind vector at level 11
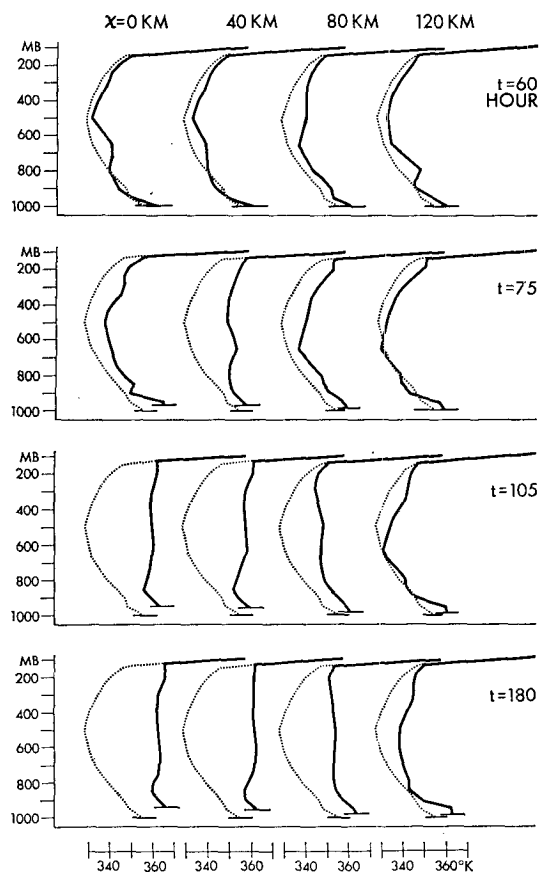at Hours 0, 45, 70, 100 and 195.

FIG. 7. Vertical distribution of equivalent potential temperature at 0, 40, 80, 120 km radii at Hours 60, 75, 105 and 180. The dotted curve shows the initial distribution.

inflow below. In period D2, very weak outflow appears at around 500 mb. This outflow area moves down in the mature stage to 700 mb and extends outward to several hundred kilometer radius. In period M1, a secondary circulation regime develops at the upper levels; it weakens slightly at M3. It may be of interest to note that this secondary flow seems to have little effect on the distribution of the azimuthal component of the wind.

The vertical cross sections of the vertical p-velocity in periods P2, D1 and M1 are shown in Fig. 10. The upward motion intensifies during the pre-deepening stage. The minimum ω, i.e., the maximum upward motion, in periods P1, P2 and P3 are -6.8, -15.9 and -31.7, respectively, in units of 10^{-3} mb s^{-1}. The position of these minima moves inward from 190 km at P1 to 130 km at P3. It is located inside the position of maximum azimuthal flow. The intensification of upward motion and the inward movement of the position of minimum ω continues through the deepening stage. In period M1, the minimum ω is -81.5×10^{-3} mb s^{-1} at 50 km radius. It weakens later and the minimum at M3 is -70. The fluctuation of intensity of vertical motion is large. The extreme instantaneous value (-168.2

$\times 10^{-3}$ mb s^{-1}) is observed at Hour 136. In the mature stage, an area of downward motion with a mean maximum value about 2×10^{-3} mb s^{-1} encircles the area of strong upward motion. In the outer area beyond 1000 km, very weak subsidence predominates and mean upward motion appears only at radii between 1200 and 1500 km and in the layer between 600 and 850 mb.

In the present model, a mean downward motion near the center, which is a characteristic structure of the eye of a tropical cyclone, is obtained only at the deepening stage. In the mature stage, the vertical motion near the center occasionally becomes downward, but it is upward on the average. The 20 km resolution of the present model is apparently inadequate to resolve the detailed structure of the core region.

Shrinking of the vortex during the pre-deepening and deepening stages is studied by examining the radial distance at which the maximum of a certain quantity occurs. Fig. 11 illustrates such positions in periods P1 through M3 for v_8 and v_{11} (the azimuthal motion at levels 8 and 11, respectively), u_{11} (the radial motion at level 11), and the vertical mean of ω. The inward movement of these positions is clearly seen. As mentioned before, the position of maximum v_{11} is inside the radius of maximum v_8. In other words, a line connecting the maximum v at each level bends inward in a shallow layer above the surface (Fig. 8). It is also seen in Fig. 11 that the maximum in upward motion tends to be observed inside the radius of the strongest inflow at the surface.

7. Analysis of the temperature field

a. Evolution of the temperature field

As described in the preceding section, the central part of the tropical cyclone, in the mature stage, is no longer in a state of conditional instability.

Fig. 12 shows a vertical temperature cross section and its difference from that at 1500 km radius for period M1. It is seen that fairly warm air is confined within the radius of 100 km. The freezing temperature near the center is observed at 460 mb in contrast to 550 mb beyond 200 km radius. The largest temperature deviation found in the right part of Fig. 12 is greater than 14 K and is located at the center of the warm core in the upper central area. Another relatively warm area is observed at the lower levels outside 100 km, making a relatively cool central area. A narrow and tall warm air column, which is observed at the center of actual hurricanes (e.g., Hawkins and Rubsam, 1968) is almost missing in the present result. This is related to the lack of a distinct eye. In Fig. 12, a relatively cold area is seen at levels 2 and 3. Cold temperature in the upper troposphere and lower stratosphere over hurricanes has been pointed out by Koteswaram (1967).
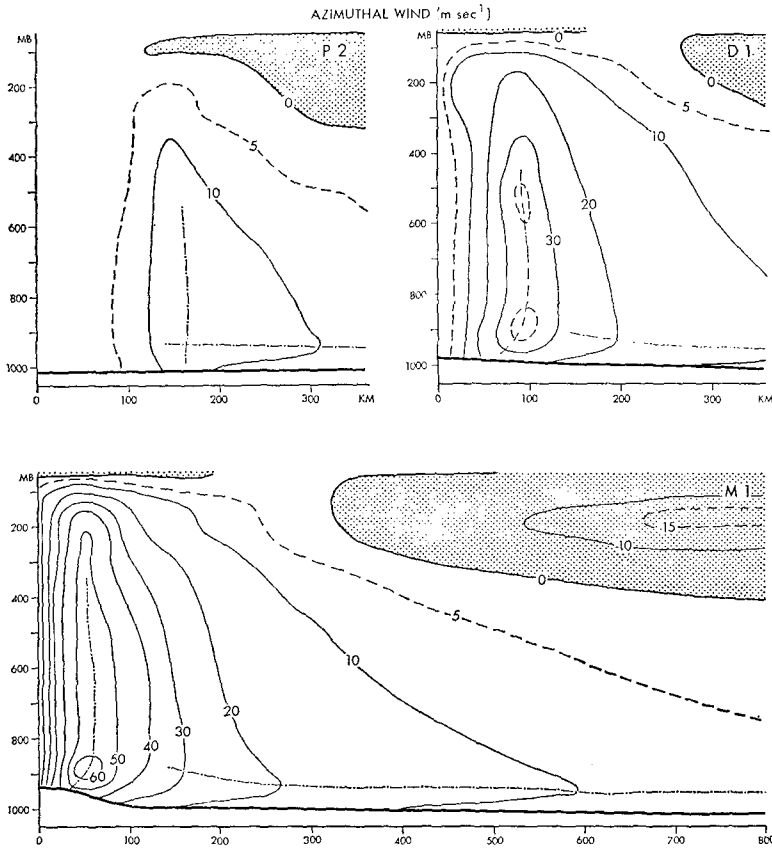
AZIMUTHAL WIND 'm sec¯¹]

FIG. 8. Vertical cross sections of azimuthal component of wind for periods P2, D1 and M1. Flow is anticyclonic in the shaded area. Dash-dotted lines show the ridge lines in the distribution.

The radial distributions of the temperature change from the initial time to periods P2, D1, M1 and M3 at 100, 300, 500, 700 and 900 mb are shown in Fig. 13. The development of a warm core at 300 and 500 mb during the periods D1 through M1 is abrupt. Generally speaking, the temperature keeps increasing at all levels. It should be noted that the effect of radiation is not included in the present model.

b. Budget of heat

The local change of temperature in the σ-coordinate system may be written as

$$\frac{\partial T}{\partial t} = TA + TB + TC + TD + TE, \qquad (7.1)$$

where:

TA   change due to large-scale advection
TB   dry adiabatic change $[= (RT\omega)/(c_p p)]$
TC   effect of horizontal diffusion $[= {}_{\rm H}F_T/p_*]$
TD   effect of vertical diffusion $[= {}_{\rm V}F_T/p_*]$
TE   change due to condensation-convection
     $[= \mathrm{QCON}/p_*]$.

In general, the change of a quantity α due to large-scale advection can be estimated from $[-D(\alpha) -\alpha \partial p_*/\partial t]/p_*$, which is identical to $-u(\partial \alpha/\partial x) -\dot{\sigma}(\partial \alpha/\partial \sigma)$.

The heat budget of the whole system depends only on the mass integral of the terms TB, TD and TE, as the integrals of terms TA and TC vanish.

The release of the latent heat, i.e., TE, is the only major source for the increase of total potential energy, or mean temperature, of the present model. The conversion to kinetic energy, TB, and the exchange of sensible heat at the sea surface, TD, are small as compared to TE. Radiation effects are not included in the model, as mentioned before. Consequently, the mean total potential energy increases from 2.679×10^{12} ergs cm^{-2} at Hour 0 to 2.710 at Hour 240.

In the beginning of the integration, the factor TD gives differential heating since the initial surface wind is not uniform. At Hour 1, the temperature difference between 210 and 1500 km radii at level 11 is 0.22 K. Then, as the frictional convergence develops in the boundary layer, the terms TA, TB and TE become important in the local heat budget.
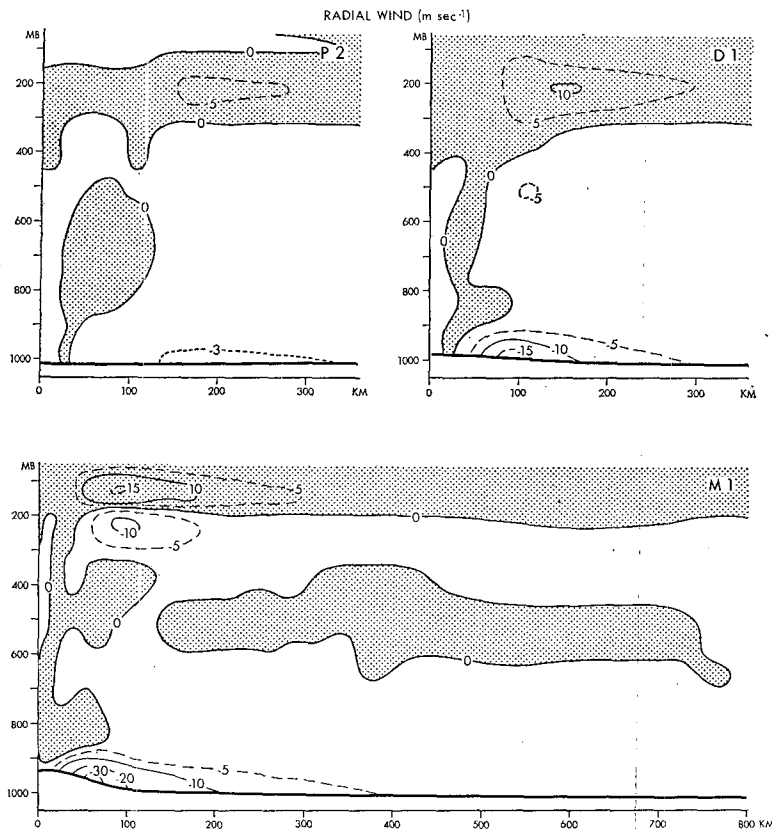
FIG. 9. Vertical cross sections of radial component of wind for periods P2, D1 and M1. Area of outflow is shaded.

During the pre-deepening and the deepening stage, the warming takes place at radii where the mean upward motion is strong. In such a region, TA is usually positive at all levels. At the lower levels, the horizontal convergence of sensible heat makes a positive contribution to TA, while at the upper levels, the vertical transport of sensible heat from below overcompensates the cooling due to horizontal flux divergence of heat. The adiabatic cooling, TB, in this region makes TA+TB negative, i.e., the total explicit effect of large-scale motion is to lower the temperature. The diffusion effect, TC+TD, is generally very small. Thus, the imbalance between TA+TB and TE determines the temperature tendency. In order for local warming to occur, TE should be large enough to surpass the cooling effect due to TA+TB. In other words, the thermodynamical state has to be favorable for the sufficient amount of condensation to take place. Especially, the air has to be humid enough. Since the mixing ratio at the low level is more or less bounded by sea surface temperature, a tropical cyclone can develop only over a warm ocean as pointed out by Palmén (1948). The stratification of the atmosphere is another control factor for the process of convection and hence for the development of tropical disturbances.

The vertically averaged values of each term in the heat equation in the early deepening stage (D1) at the 70 km radius, where the precipitation is largest, are as follows (units, 10^{-5} K s^{-1}):

$TA = 383.0$, $TB = -556.8$, $TC = 1.2$, $TD = -0.3$,
$TE = 176.7$
$Sum = 3.8$.

Thus a small but important difference ($\sim 3 \times 10^{-5}$ K s^{-1}) between TE and TA+TB is found. A similar result has been obtained in the analysis of typhoon Doris (Yanai, 1961a).

In the later period of the development stage, the values of TA, TB and TE at the radius of maximum precipitation are more than doubled as compared in the early period. This results from a feedback process which intensifies the solenoidal field and the radial-vertical circulation. Also in this later stage, TE is larger than the negative tendency due to TA+TB.

In Fig. 14, cross sections of TA+TB, TC, TD and TE for the period M1 are shown. The effect of large-scale motion, i.e., TA+TB, is slightly overbalanced by TE. The net warming effect obtained from TA+TB+TE is canceled by the diffusion effect due to TC+TD, as far as the present model is con-

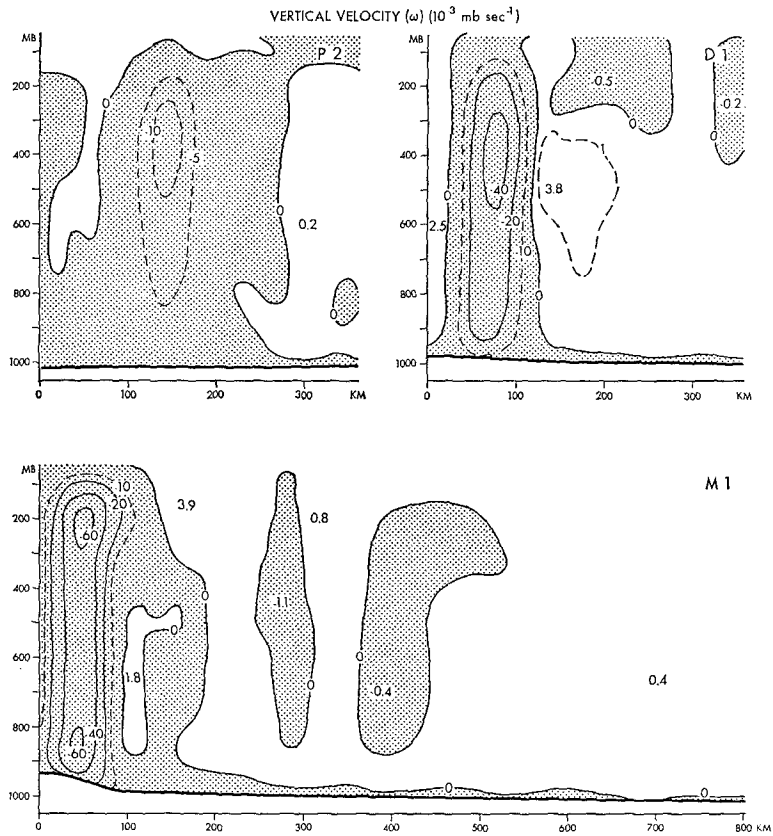VERTICAL VELOCITY (ω) $(10^{-3}$ mb sec$^{-1})$

FIG. 10. Vertical cross sections of vertical motion for periods P2, D1 and M1.
Area of upward motion is shaded.

cerned. An exception to the above-mentioned feature is found in a shallow layer above the surface. In this layer, TE is smaller than the cooling due to TA+TB. The warming effect by the vertical diffusion process, TD, is important for the heat balance in this thin layer.

As mentioned above, TE in the free atmosphere of the inner region is more or less balanced by TA+TB. It should be noted here that the adiabatic cooling TB is of larger magnitude than TE. For example, the vertical mean of TB and TE at 50 km radius in the period M1 are −1172.0 and 373.5, respectively. On the other hand, the value of TA of 809.7 yields −362.3 for TA+TB. This suggests the importance of the warming effect due to the influx of warm air at the low levels and the outflow of air with less sensible heat at the upper levels.

Other factors, which might contribute to the heat budget in the inner region but are not considered in the present model or cannot be treated with the present horizontal resolution, are the heating due to internal dissipation (Riehl and Malkus, 1961) and the outward advection of warm air from the eye which has been hypothesized recently (Gray and Shea, 1973).

8. Analysis of the moisture field

a. Evolution of the moisture field

The formation of a warm core in the inner region of a tropical disturbance is accompanied by an increase of moisture content.
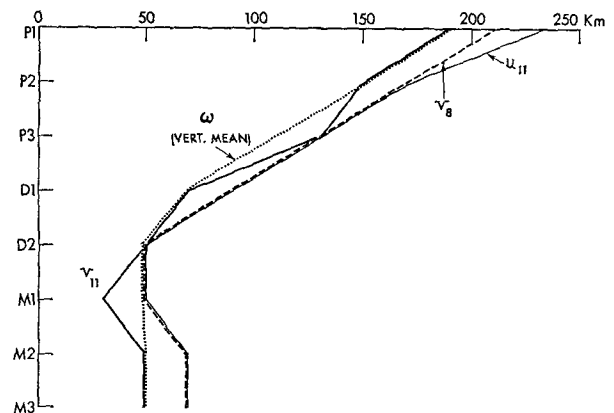

FIG. 11. Radial distance of maxima in u_{11}, v_8, v_{11} and vertical mean ω as a function of the growth stage.
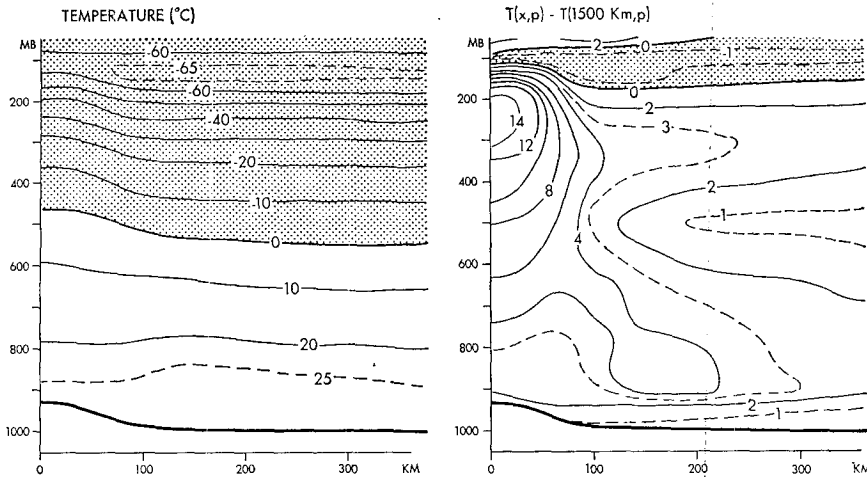
FIG. 12. Vertical cross section of temperature at period M1 (left, °C) and its difference from the temperature at 1500 km (right, K). Areas of negative temperature and negative difference are shaded.

Fig. 15 shows the distribution of mixing ratio and relative humidity for periods P2, D1 and M1. For period P2, the relative humidity in the middle and
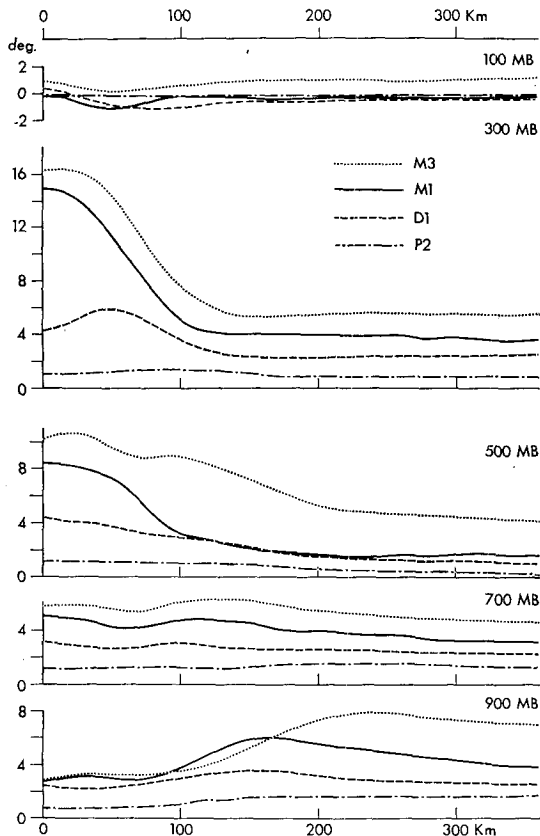

FIG. 13. Radial distribution of temperature change from initial value to that for periods P2, D1, M1 and M3 at 100, 300, 500 700 and 900 mb levels.

upper layers is highest at 140 km. It is also seen that moist air is flowing out at the upper levels. In the deepening stage, an air column at a smaller radius is quite moist. A moist layer extends along the 200-mb level. Relative humidity is low near the center, especially at the upper levels, because of the smallness of the mixing ratio. Another low relative humidity area surrounds the middle and lower part of the moist column. At the mature stage, both absolute and relative humidity are high in the central region. Relative humidity between 120 and 300 km is less than 50% except in the boundary layer. This is not because of a small mixing ratio but rather due to the relatively high temperature.

b. *Budget of water vapor*

The local change of mixing ratio of water vapor is governed by

$$\frac{\partial r}{\partial t} = \text{RA} + \text{RB} + \text{RC} + \text{RD}, \qquad (8.1)$$

where:

RA   change due to large scale advection
RB   effect of horizontal diffusion $[= {}_{\text{H}}F_r/p_*]$
RC   effect of vertical diffusion $[= {}_{\text{V}}F_r/p_*]$
RD   change due to condensation-convection process
       $[= \text{RCON}/p_*]$.

The time change of the moisture content for the whole system is determined from the mass integrals of RC and RD, which yield the total evaporation and total precipitation, respectively. As shown in Fig. 4, total precipitation is generally larger than total evaporation in the present experiment. Consequently,
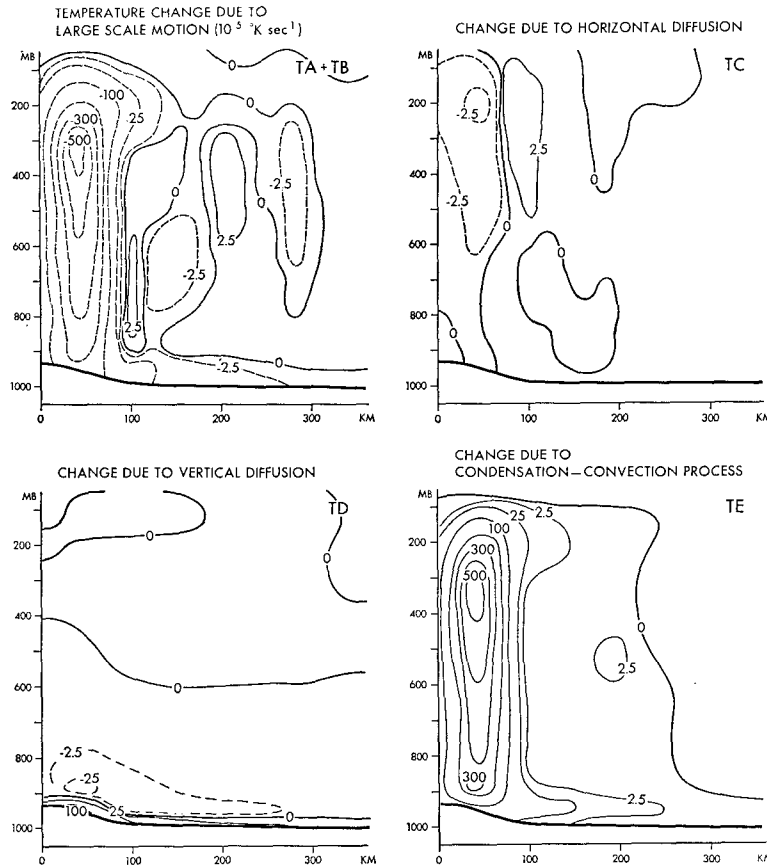
FIG. 14. Vertical cross sections of heat budget components at period M1: temperature changes (all units 10^{-5} K s^{-1}) due to advection and dry adiabatic change (TA+TB), horizontal diffusion (TC), vertical diffusion (TD) and condensation-convection (TE).

the mean precipitable water decreases from 5.142 g cm^{-2} at Hour 0 to 4.299 g cm^{-2} at Hour 240.

In the pre-deepening and deepening stages, moisture added to the air column at the radius of large precipitation slightly exceeds loss due to precipitation. For instance, for period P2, the vertical mass integral of RA+RB+RC and RD at 150 km, where the rainfall intensity corresponds to 5.6 mm h^{-1}, are 1.809 and -1.554 (10^{-4} g cm^{-2} s^{-1}), respectively. Those values for period D1 at 70 km, where the rainfall intensity is 25 mm h^{-1}, are 7.269 and -6.975. The supply of moisture to the above places occurs primarily by the advection, i.e., RA. The evaporation at the ocean surface is an additional source of moisture which diffuses upward. At any rate, it is important that the air which is advected to the places of intense rainfall be sufficiently moist before it arrives there. Otherwise, a warm moist core which is indispensable to the development and maintenance of a tropical cyclone may not be formed.

The spacial distributions of RA, RB, RC and RD for period M1 are shown separately in Fig. 16. Within

the radius of 100 km, the strong upward motion transports moisture, yielding a maximum RA at middle levels. At lower levels, the vertical export of moisture is surpassed by the import by the horizontal flow. Thus, another maximum RA is observed at a low level at 50 km. The evaporation (RC) also contributes as a source of moisture for the low levels. The water vapor that converges into a central region or is supplied from below is almost completely removed by the condensation (RD). A small amount of water vapor is transported outward by horizontal diffusion (RB).

There exists a very thin layer of positive RA along the surface beyond 100 km. This is due to the horizontal convergence of moisture. Above it, an area of negative RA is caused by the subsidence of dry air. As discussed by Ooyama (1969a), such a drying tendency in the outer area is cancelled largely by the moistening due to evaporation and vertical diffusion processes (RC) as seen in Fig. 16.

The importance of evaporation (the term RC in the water vapor budget) is explicitly found when the
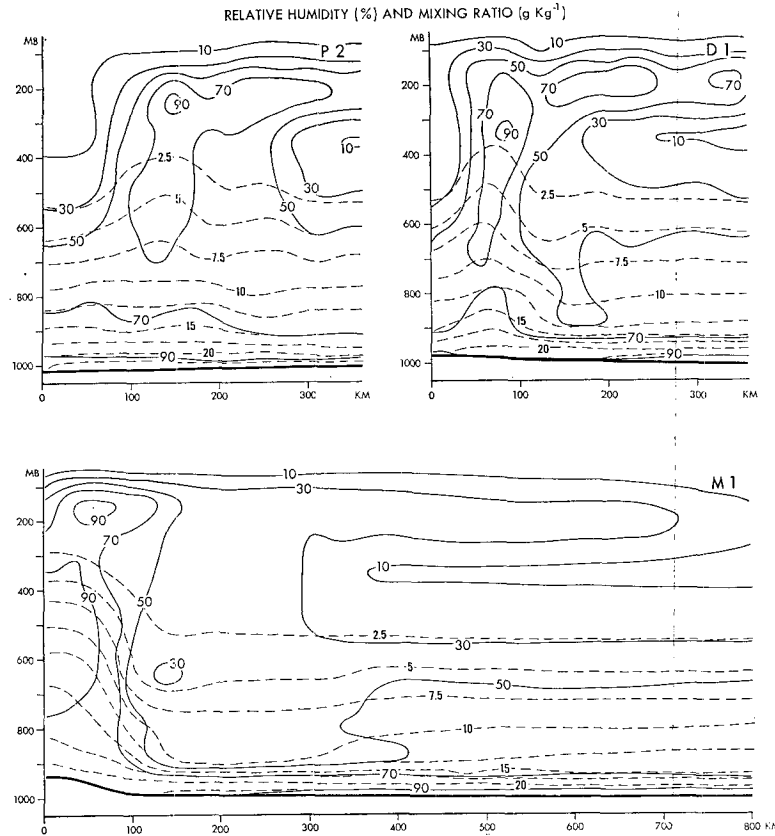
RELATIVE HUMIDITY (%) AND MIXING RATIO (g Kg⁻¹)

FIG. 15. Vertical cross sections of relative humidity (solid lines, percent) and mixing ratio (dashed lines, g kg⁻¹) at periods P2, D1 and M1.

budget is examined for a domain which includes the above-mentioned outer area. For example, the mass-weighted averages of each term of (8.1) for the 500 km domain for the period M1 are

$$RA = 19.69, \quad RB = 0.02, \quad RC = 5.18, \quad RD = -24.52,$$

the units being 10^{-6} g cm^{-2} s^{-1}. Thus evaporation provides the air with a significant amount of water vapor while it travels across the outer area. If the domain of integration is reduced to the inner area, the relative magnitude of RC as compared with RA and RD becomes very small. Thus, as mentioned by Malkus and Riehl (1960), the contribution of evaporation in the inner area to the water budget appears to be insignificant. However, it will be pointed out in Section 13 that a seemingly negligible amount of evaporation in the inner area can play a crucial role in the energetics of a tropical cyclone.

In the present model, the effect of condensation-convection processes, i.e., RD, is estimated by a scheme of moist convective adjustment. It may be of interest to examine the relation between RD and the moisture convergence in the boundary layer. In Fig. 17, the influx of moisture below the level $\sigma = 0.86$ across the cylindrical wall at 100 km and the mean precipita-

tion rate within 100 km are shown in arbitrary units. The correlation between the two quantities is 0.75. This result means that, in the inner region of a tropical cyclone, the behavior of the parameterization of convection in the present model may be similar to that of other schemes in which RD is directly related to the upward latent energy flux at the top of the boundary layer.

9. Budget analysis of relative angular momentum

a. General feature of time variation

The relative angular momentum about the cyclone axis may be defined by multiplying the arm length x by the relative azimuthal velocity v, i.e., xv. If v is replaced by the absolute azimuthal velocity, $v+xf/2$, the absolute angular momentum A is obtained, i.e., $A = xv + x^2f/2$. The quantity $x^2f/2$ may be called the earth angular momentum.

The area mean of the vertical mass integral of relative angular momentum of the present model decreases from 0.552 at Hour 0 to −0.736 at Hour 240, in units of 10^{13} g s^{-1}. Estimates of this same quantity at the different periods are listed in the second column of Table 4.
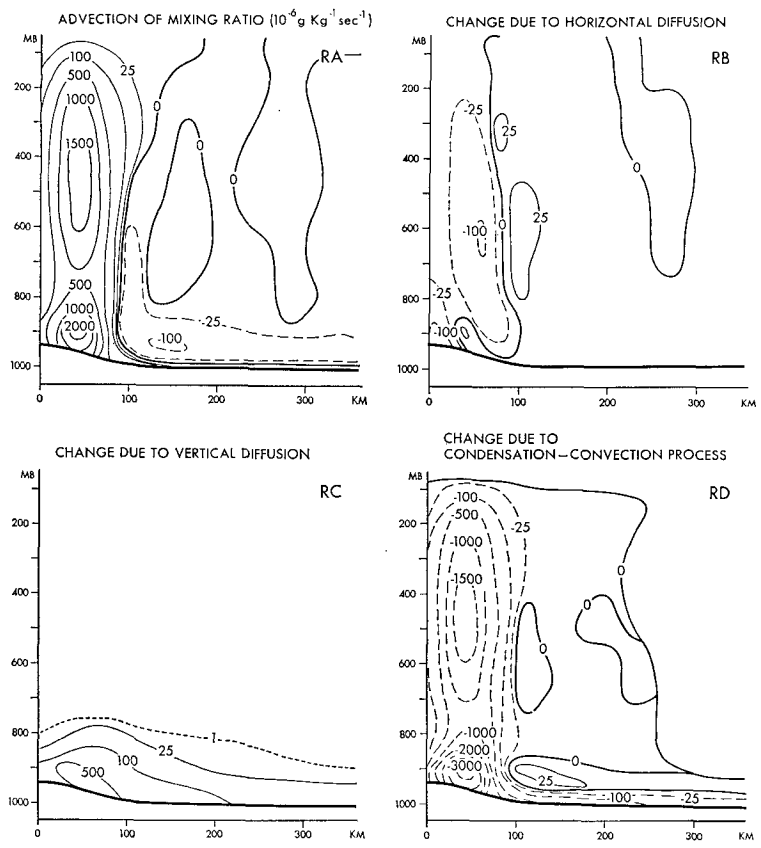
FIG. 16. Vertical cross sections of water vapor budget components at period M1: mixing ratio changes (all units 10^{-6} g kg^{-1} s^{-1}) due to advection (RA), horizontal diffusion (RB), vertical diffusion (RC) and condensation-convection (RD).

The local change of xv is given by

$$\frac{\partial xv}{\partial t} = MA + MB + MC + MD, \qquad (9.1)$$

where:

MA   change due to large-scale advection of relative angular momentum

MB   change due to large-scale advection of earth angular momentum

MC   change due to horizontal diffusion of relative angular momentum $[= x_H F_v/p_*]$

MD   change due to vertical diffusion of relative angular momentum $[= x_V F_v/p_*]$.

Eq. (9.1) may be considered as the equation for the absolute angular momentum, since $\partial(x^2 f/2)/\partial t$, which
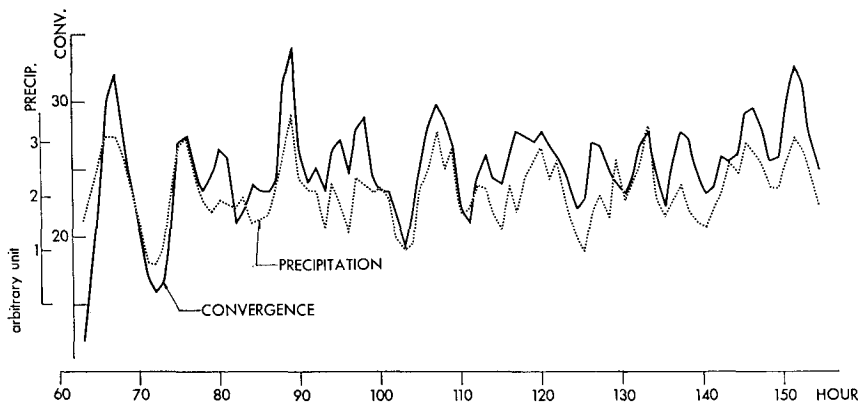

FIG. 17. Horizontal convergence of water vapor below the level $\sigma = 0.86$ into the 100 km radius region and area-mean precipitation in that area.

TABLE 4. Area mean of vertically integrated relative angular momentum (r.a.m.) and the rate of change due to the surface stress.

Period	Area: 0–2000 km		Area: 0–500 km	
	Mean r.a.m. ($\times 10^{13}$ g s^{-1})	Change in r.a.m. due to surface stress ($\times 10^{7}$ g s^{-2})	Mean r.a.m. ($\times 10^{13}$ g s^{-1})	Change in r.a.m. due to surface stress ($\times 10^{7}$ g s^{-2})
$t=0$	0.552		1.071	−1.065
P1	0.544	−0.170	1.071	−1.065
P2	0.518	−0.398	1.176	−1.768
P3	0.473	−0.625	1.626	−2.774
D1	0.429	−0.875	2.146	−4.220
D2	0.385	−1.047	2.387	−5.377
M1	0.242	−1.404	2.593	−7.368
M2	−0.227	−2.069	2.903	−9.394
M3	−0.671	−2.353	2.911	−8.731

is always zero, can be added to the left-hand side of (9.1). For the term MB we have the identity

$$\mathrm{MB}=\left[-D\left(\frac{f}{2}x^2\right)-\frac{f}{2}x^2\frac{\partial p_*}{\partial t}\right]\bigg/ p_*,$$

$$= -xfu. \tag{9.2}$$

Thus, the term MB may be interpreted either as a transformation of earth angular momentum to relative angular momentum through the advection process, or as the torque due to the azimuthal component of the Coriolis force.

The following equation is easily derived from (9.1):

$$\frac{\partial}{\partial t}(p_*A)= -D(A)-x_{\mathrm{H}}F_v-x_{\mathrm{V}}F_v. \tag{9.3}$$

When (9.3) is integrated over the entire domain, the first and the second terms on the right-hand side vanish. Consequently, as we would expect, the change of total absolute angular momentum is controlled solely by the exchange of momentum at the earth's surface.
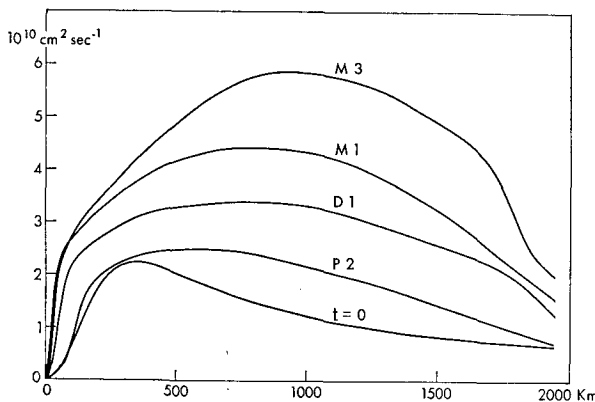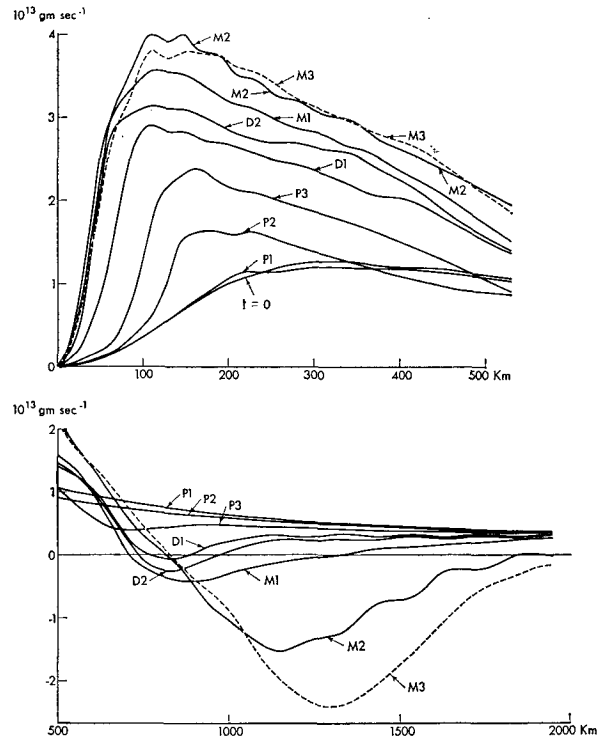

FIG. 19. Radial distribution of vertical mass integral of relative angular momentum at different periods.

In the present experiment, the change in total earth angular momentum due to redistribution of mass is very small. In other words, the vertical mass integral of the term MB is negligible at any radius. Therefore, the decrease of total relative angular momentum should be highly correlated to the mass integral of MD, i.e., the loss by the surface stress. The third column of Table 4 shows the area mean of the loss of relative angular momentum by surface stress. Note that the mean loss keeps increasing with time, sug-

FIG. 18. Radial distribution of relative angular momentum at level 11 at $t=0$ and for periods P2, D1, M1 and M3.
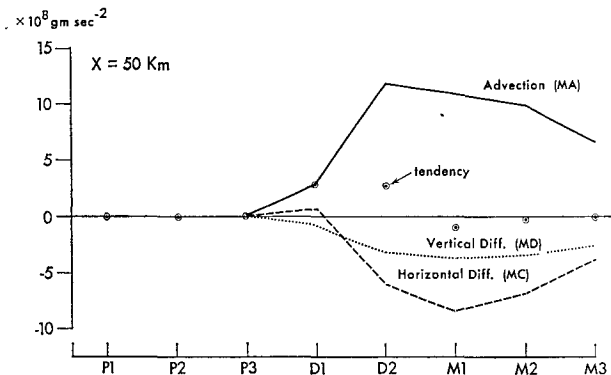

FIG. 20. Budget components for vertical mass integral of relative angular momentum at 50 km radius at different periods: changes due to advection MA, horizontal diffusion MC, vertical diffusion MD, and the total (tendency, open circles with dots).

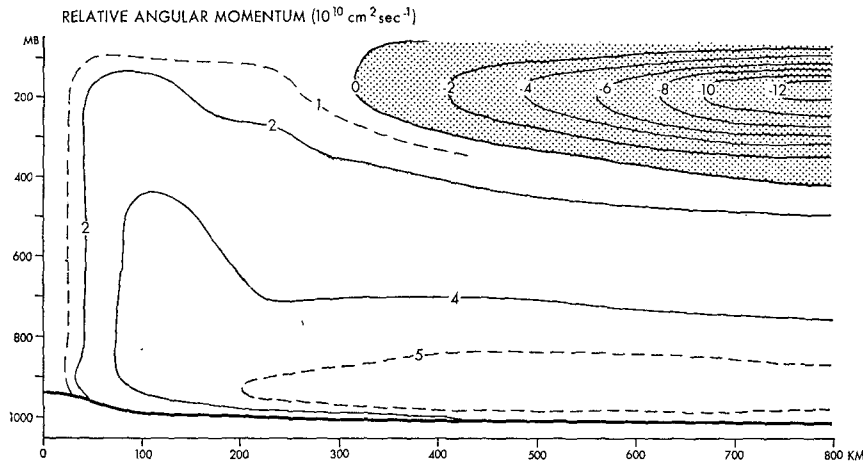RELATIVE ANGULAR MOMENTUM (10^{10} cm^{2}sec^{-1})

FIG. 21. Vertical cross section of relative angular momentum at period M1.
Area of negative momentum or anticyclonic flow is shaded.

gesting the nonsteadiness of angular momentum field even at the mature stage. To examine this, the radial distribution of xv at level 11 is shown in Fig. 18 for the different periods. Despite the existence of a sink of xv at the surface, xv at level 11 increases at all radii. It is not known whether or not a surface anticyclonic flow would eventually appear at large radii to make up the angular momentum budget in a closed domain, if the present integration had been continued. This feature of the budget may be also influenced by the initial conditions of the integration.

The time variation of the radial distribution of vertical mass integral of relative angular momentum is shown in Fig. 19. Within the radius of about 500 km, a quasi-stationary state seems to be reached at the late mature stage. This is also seen in the fourth column of Table 4, which gives the mean relative angular momentum within 500 km at the different periods. The mean loss at the bottom of the air column is also listed in the last column of the same table. In the outer region, the vertical integral of xv decreases during the integration period. Since xv increases at the lower level as shown in Fig. 18, xv should decrease at the upper levels and an anticyclonic circulation should develop there.

b. Increase in the central area

As shown in Fig. 19, the relative angular momentum of an air column near the center increases sharply in the deepening stage. At 50 km radius the terms in the equation for xv are vertically integrated to see the contribution from each term. The computed results at different periods are presented in Fig. 20. In the pre-deepening stage, all terms are too small to show in the figure. The term MB, i.e., the torque due to

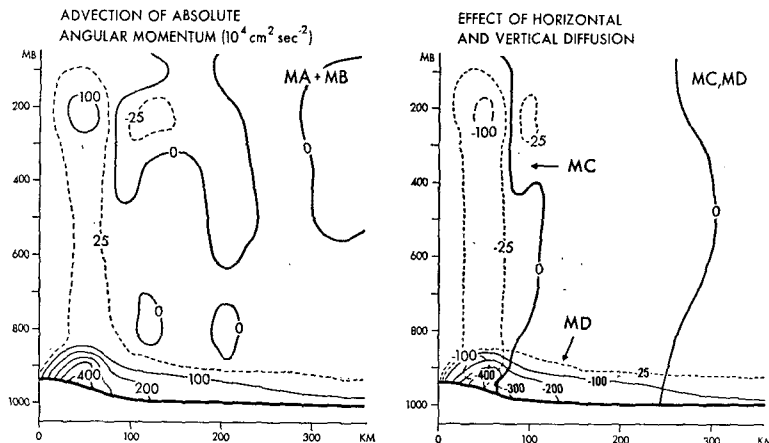FIG. 22. Vertical cross sections of relative angular momentum budget components at the period M1: changes (all units 10^4 cm^2 s^{-2}) due to advection of relative and earth angular momentum (MA+MB), and horizontal and vertical diffusion (MC and MD).
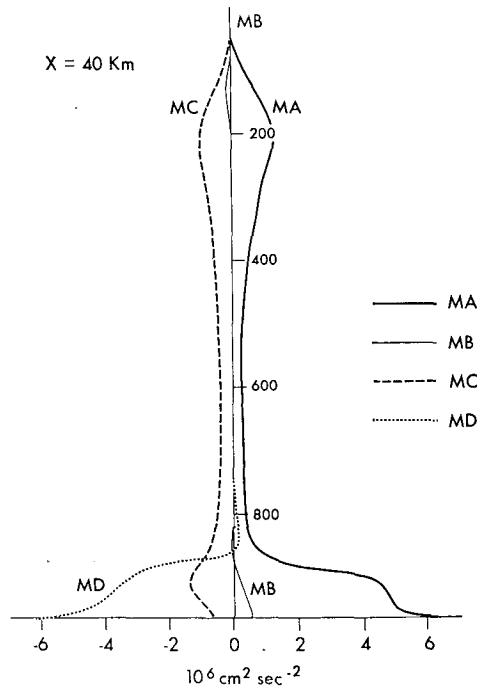
FIG. 23. Vertical distribution of relative angular momentum budget components at the 40 km radius for period M1.

the Coriolis force, gives a positive contribution at the lower levels and a negative contribution at the upper levels. However, its vertical integral is negligibly small, because a net mass flux through a given radius is almost zero.

It is clearly seen in Fig. 20 that the net convergence of relative angular momentum (MA) is a cause of the positive tendency in periods D1 and D2. A more detailed analysis shows that MA is positive throughout the column. At upper levels, the transport of xv from below overcompensates the horizontal divergence of xv. At lower levels, the horizontal convergence of xv is larger than its export to the upper levels. As the radial gradient of xv increases, the effect of horizontal diffusion (MC) becomes large. This effect, together with that of vertical diffusion (MD), counteracts the increase of relative angular momentum in the central area.

c. Budget at the mature stage

The distribution of relative angular momentum at the period M1 is shown in Fig. 21. As mentioned before, the outer portion of this field is not quasi-stationary. Within about 100 km, the vertical variation of xv is very small. Beyond 300 km, the contour lines run nearly horizontally, which means that v is almost inversely proportional to x. At the lower levels beyond the 500 km, v decreases slightly faster than x^{-1}. The same feature is discussed by Yamasaki (1968b) with respect to the surface wind. At the upper levels,

an anticyclonic flow exists outside a radius of 300 km. The zero line, where v vanishes, intersects the lateral boundary at about the 450-mb level. The minimum value of xv for this period is located at the 800 km radius at the 150-mb level.

The budget of xv during the period M1 is illustrated in Fig. 22, where the effects of large-scale flow (MA+MB) and of diffusion (MC and MD) are shown separately. In the central area, MA alone is positive at all levels. The radial flow gives horizontal convergence of xv at the lower levels and divergence at the upper levels. The associated upward motion transports xv from the lower levels to the upper levels. The net effect of the horizontal and vertical advection results in an increase of xv at all levels. Beyond about 600 km, MA is weakly negative. The effect of MB depends on the radial flow. Roughly speaking, it leads to a decrease of xv at the upper troposphere and an increase at the lower levels, especially in the boundary layer. In summary, the two effects MA and MB have the same sign in the inner lower part and the outer upper part of the domain and opposite sign elsewhere. The left part of Fig. 22 shows the combined effect, MA+MB.

As seen in Fig. 22, the effect of MA+MB within the 100 km radius is balanced by MC in the free atmosphere and by MC+MD in the boundary layer. As an example, the vertical distribution of each term at 40 km is presented in Fig. 23. At this particular radius, MB is small as the radial flow is weak. Although in the present model the lateral stress plays a significant role at the mature stage in the inner area, in agreement with Riehl and Malkus's analysis (1961) of hurricane Daisy at the well-developed stage, its importance is still not completely proved. A balance without MC may be possible if the motion field changes slightly so that MA+MB vanishes in the free atmosphere of the central area. Transport of momentum by cumulus convection may be another mechanism to be considered as pointed out by Gray (1967).

d. Transport of angular momentum

Next, the gross features of the flow of angular momentum within the whole domain for period M1 is investigated. The total domain is divided into annuli by vertical walls at 100, 200, 300, 400, 500, 1000 and 1500 km radii. Each annulus is cut at the middle level so that the upper and the lower rings have the same mass. The transport of relative angular momentum, of earth angular momentum, and the diffusive flux of relative angular momentum across the vertical and horizontal boundary of each ring are estimated separately and shown in Fig. 24 by the solid, dashed and dotted arrows. In each sub-domain, a net gain as well as area-mean rate of increase in absolute angular momentum are presented. For all practical purposes, those two numbers show the variation of relative
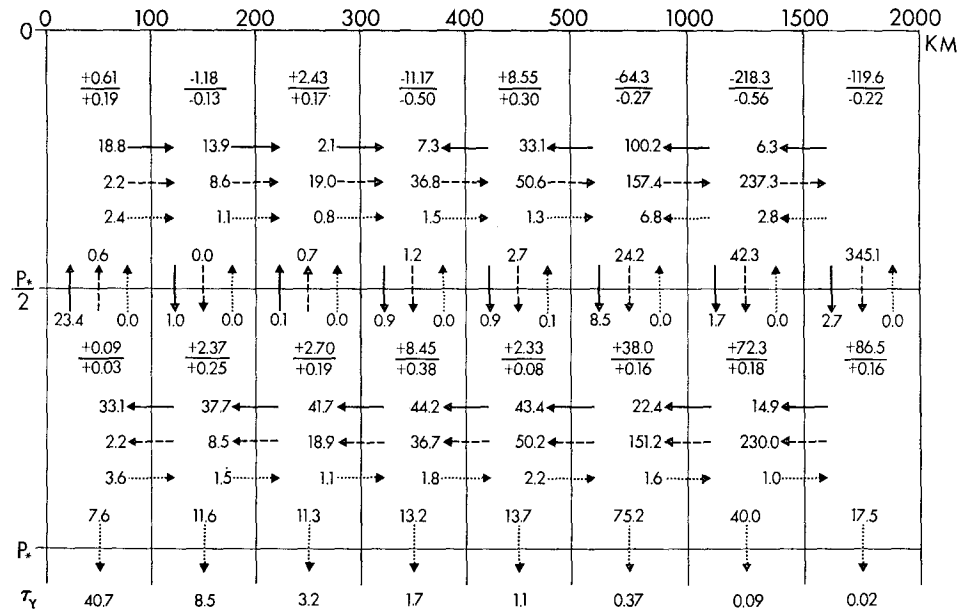
FIG. 24. Transport of relative angular momentum (solid arrows), earth angular momentum (dashed arrows) and diffusive flux of relative angular momentum (dotted arrows) across the boundaries of subdomains (all units 10^{22} g cm^2 s^{-2}). Two numbers separated by a horizontal line in each box show net gain of absolute angular momentum (upper number, 10^{22} g cm^2 s^{-2}) and area mean rate of change (lower number, 10^8 g s^{-2}). Area-mean tangential stress (dyn cm^{-2}) is shown at the bottom of the figure.

angular momentum since the change of earth angular momentum due to the redistribution of mass is negligible. The quantity at the bottom in Fig. 24 indicates the area-mean tangential stress.

Relative angular momentum is transported inward in the lower layer. The outward flux at the upper inner region is smaller than the inflow in the lower region. The inward transport at the upper outer part is due to the outward flux of anticyclonic momentum. In the innermost column, the relative angular momentum of the upper portion is maintained by a large upward transport of cyclonic momentum across the middle level.

Horizontal transport of earth angular momentum is directed inward at the lower part and outward at the upper part. They almost cancel each other, as the air mass distribution changes very little with time. The downward transport of earth angular momentum across the middle level is very large in the outer region. It contributes both to the increase of relative angular momentum in the lower part and to the development of the anticyclonic circulation in the upper part.

As discussed earlier, the lateral shear is important for the angular momentum balance in the inner region, as far as the present model is concerned. The vertical diffusion at the middle level is negligible.

The model as a whole loses absolute angular momentum through the surface stress. Hawkins and Rubsam (1968) made a budget analysis of relative angular momentum of hurricane Hilda. The mean

tangential stress between the 18.5 to 37 km radii was estimated to be 52 dyn cm^{-2}. In the present model, the average within 100 km radius is 40.7 dyn cm^{-2} while the maximum of 72.9 dyn cm^{-2} occurs at 50 km.

Palmén and Riehl (1957) discussed the flux of angular momentum within 6° radius in a mean tropical cyclone. A difference between their result and the present one is that their angular momentum balance requires a large amount of upward eddy flux of angular momentum at middle levels whereas the present budget within 500 km radius does not need a strong vertical flux except for the innermost column. The air-sea exchange of relative angular momentum in the present storm is smaller than their estimates. In spite of these differences, one of the conclusions of Palmén and Riehl's (1957) analysis [as summarized by Palmén and Newton (1969)] also applies to the present model: that is, the inner region of a tropical cyclone is a sink region for angular momentum that was originally imported from the outer region. For instance, the budget for a column of 500 km radius, in which the mean relative angular momentum is 2.59×10^{13} g s^{-1}, consists of the import of relative angular momentum, the import of earth angular momentum, and the changes due to the surface and lateral stress; the respective values for these four terms are 9.81, -0.05, -7.37 and -0.45×10^7 g s^{-2}.

10. Budget analysis of relative vorticity

In this section, the evolution of the vorticity field is analyzed using the conventional pressure coordinate
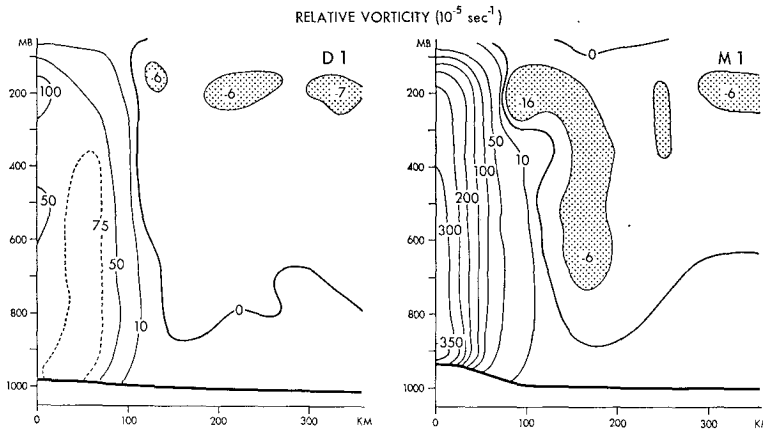
RELATIVE VORTICITY (10^{-5} sec^{-1})

FIG. 25. Vertical cross sections of relative vorticity for periods D1 and M1.
Area of negative absolute vorticity is shaded.

system. Data interpolation from the sigma to the pressure coordinate grid did not cause any serious numerical problems.

Since the relative vorticity in the pressure coordinate system is defined for the horizontal wind field on an isobaric surface, the vorticity equation does not include an explicit term associated with the solenoidal field on the horizontal plane. It should be noted, however, that the baroclinicity vector in the present axisymmetric model has only an azimuthal component.

a. Time variation of relative vorticity distribution

The radial-vertical distribution of the relative vorticity $\zeta[=\partial(xv)/x\partial x)]$ for the periods D1 and M1 is shown in Fig. 25. Positive vorticity is confined within

a 100 km radius except below about 800 mb. The maximum value for the period M1 exceeds 3.5×10^{-3} s^{-1}.

As the intensity of the hurricane vortex increases, an area of weak negative absolute vorticity appears in the upper troposphere of the outer region. The local effects of this negative absolute vorticity on the pattern of radial-vertical circulation will be discussed in the next section.

FIG. 27. The radial-vertical distribution of main budget components which contribute to vorticity increase (upper figure) or vorticity decrease (lower figure) during the transient stage. The terms ZA, ZB, ZC and ZD of Eq. (10.1) are indicated by dashed, thin solid, thick solid and dotted lines, respectively. Twisting effect is illustrated by two thin arrows; that is, the radial component of vortex (horizontal arrow) is converted into the vertical component (vertical arrow) by the radial difference of vertical motion.
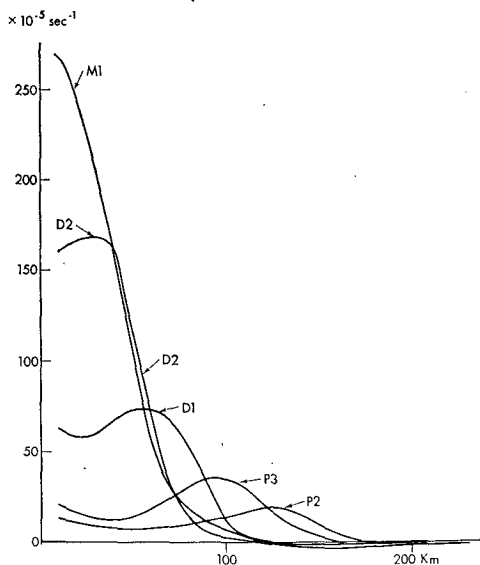

FIG. 26. Radial distribution of the vertical average of relative vorticity for periods P2, P3, D1, D2 and M1.

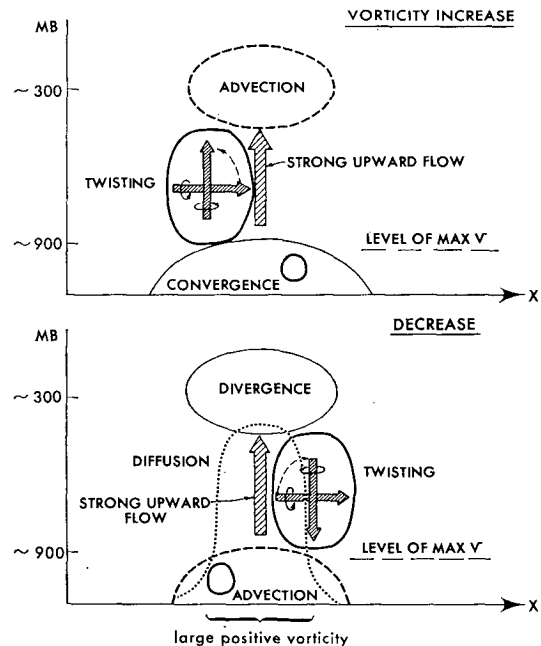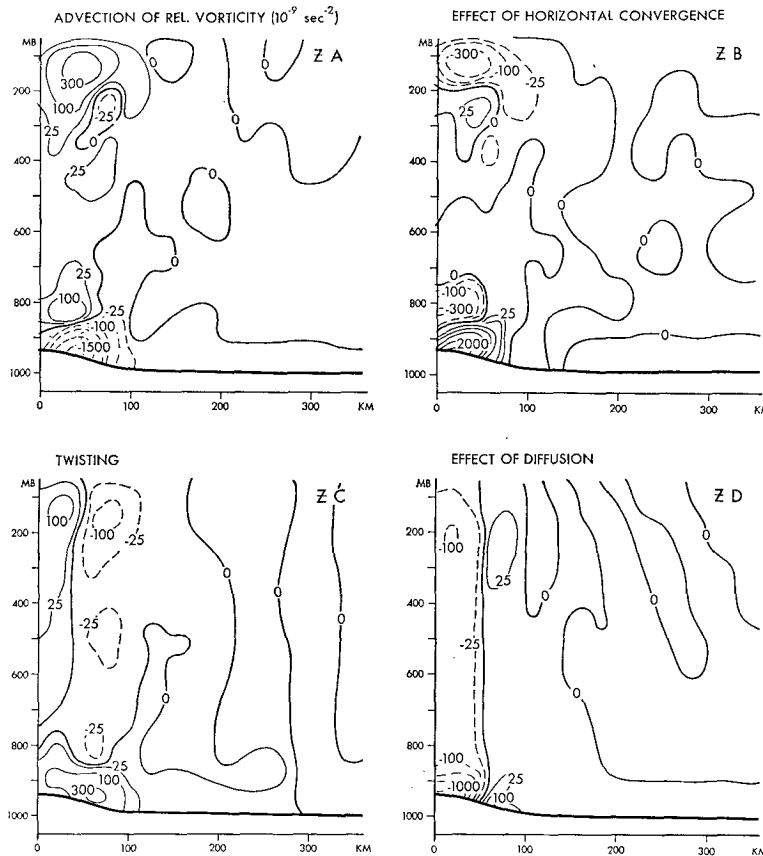Fig. 28. Vertical cross sections of relative vorticity budget components at the period M1: changes (all units 10^{-9} s^{-2}) due to advection of relative vorticity (ZA), horizontal convergence (ZB), twisting (ZC), and effect of diffusion (ZD).

Fig. 26 shows the radial distribution of the vertical average of relative vorticity for various periods. It is clearly seen that, through the pre-deepening and the deepening stages, the vorticity in the outer part of the large positive vorticity area weakens while that in the inner part increases. As a result, the vortex shrinks or the peak of the curve in Fig. 26 approaches the center until a state of quasi-equilibrium is attained.

The local rate of change of the relative vorticity ζ in the pressure coordinate system may be written as

$$\frac{\partial \zeta}{\partial t} = ZA + ZB + ZC + ZD, \qquad (10.1)$$

where:

ZA   change due to large-scale advection
$$[= -u(\partial\zeta/\partial x) - \omega(\partial\zeta/\partial p)]$$

ZB   change due to horizontal convergence
$$[= -(f+\zeta)\partial(xu)/x\partial x]$$

ZC   change due to twisting of radial component of vorticity $[= -(\partial v/\partial p)(\partial\omega/\partial x)]$

ZD   change due to frictional effect
$$[= (\partial/x\partial x)\,(x\cdot\text{azimuthal friction})].$$

The role of each term in the above equation was

investigated for various periods in the stage of vortex shrinking. The general features of the vorticity change during this transient stage are schematically summarized in Fig. 27. The upper part shows the region in the vertical section where various terms contribute significantly to an increase of relative vorticity and the lower part the region where they contribute to a decrease.

When an area of large positive vorticity is at some distance from the center, a strong upward motion is observed within that area. This vertical flow is associated with the upward transport of relative vorticity as well as the horizontal convergence in the lower layers and the divergence in the upper layers. Therefore, even though the effects of horizontal advection are also included in the term ZA, the two terms ZA and ZB tend to have the opposite sign. Inside the radius of strong upward flow, ZA is larger than ZB in the upper layer and *vice versa* in the lower layer. The importance of low-level convergence and the upward transport of vorticity has also been analyzed in the study of the formation of typhoon Doris by Yanai (1961a).

As for the twisting term, its effect of decreasing the vorticity has been pointed out by Yanai (1961a) on the basis of observed data and by Anthes (1972) in his numerical simulation experiment. In the present analysis, both the positive and negative contribution of the term ZC are stressed. As shown in Fig. 8, the azimuthal flow is maximum at around the 900-mb level. This means that the radial component of vorticity points outward in the free atmosphere and inward in the planetary boundary layer. Consequently, inside the radius of maximum upward motion, the twisting term ZC causes an increase of the vertical component of vorticity in the free atmosphere whereas it contributes to a decrease in the boundary layer. The effect is opposite in the outer region. The feature in the upper outer region agrees well with the above-mentioned analyses by Yanai and Anthes. The diffusion term ZD acts to decrease the vorticity but its role in the vorticity budget is small at the transient stage.

In summary, shrinking of the vortex is caused by the increase of vorticity inside the radius of maximum vorticity, mainly due to ZA at the upper levels and ZB at the lower levels, and its decrease in the outer region due to ZC.

b. Budget at the mature stage

The general characteristics of the budget of relative vorticity do not change materially going from transient stage to the mature stage. The factor which terminates the intensification and shrinking of the vortex is the increase of the frictional effect. Vertical cross sections of each term in the vorticity equation for the period M1 are shown in Fig. 28. The distribution of ZA reflects the vertical transport of vorticity from the boundary layer to the free atmosphere. Within the 100 km radius, ZB is negatively correlated with ZA. The term ZC is positive in the boundary layer and also inside 40 km in the free atmosphere. The term ZD represents the effect of both lateral and vertical stress. The lateral stress is a predominant component in the free atmosphere, while the vertical stress is a main factor in the boundary layer.

The distributions shown in Fig. 28 qualitatively agree with the vorticity budget analyses by Yamasaki (1968a) for his numerical model experiment. Although his results were obtained for the rapid development stage, it is unlikely that the general features will change drastically at the mature stage. Yamasaki has emphasized that the frictional effect will increase the relative vorticity near the surface in the outer region. A similar result is found in the distribution of ZD in the present experiment, though the formula used to estimate the surface stress is different from that used in his scheme.

Roughly speaking, the terms ZA and ZB are predominant in the local vorticity budget at the upper

and lower levels. The effects ZC and ZD are very important when the budget of mean vorticity of a whole air column is considered, especially inside 100 km. This is because the vertical integrals of ZC and ZD are obtained by the accumulation of relatively small values with the same sign, whereas the integrals of ZA and ZB are obtained from a sum of large values with different signs.

Fig. 29 shows the radial distribution of the vertical mean of each term for the period M1. Inside the 40 km radius, advection, horizontal convergence and twisting effects act to intensify the mean vorticity of an air column. The only counterbalancing term is the diffusion effect. At about 70 km, the tendency due to each term is reversed. In the figure, the sum of the four terms, the net effect, is also plotted. This sum does include possible truncation errors involved in the numerical analysis and does not necessarily indicate the real tendency. Actually, the net effect is too large to be taken literally as the real tendency. Nevertheless, the relative smallness of the net effect seems to indicate that Fig. 29 shows a vertically averaged state of balance of relative vorticity at the mature stage with an acceptable degree of accuracy.

11. Analysis of radial-vertical circulation

a. Evolution of radial-vertical circulation

In the present numerical experiment, there exists no radial-vertical circulation at the beginning of the integration. The initial axisymmetric vortex, which is
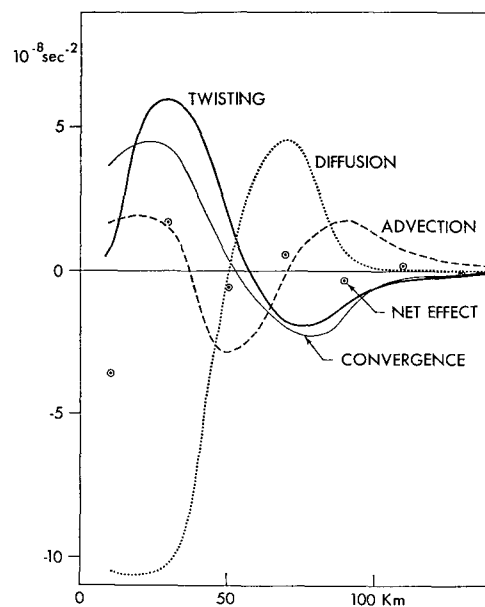

Fig. 29. Radial distribution of the vertical mean of the relative vorticity budget components at the period M1: changes due to advection (dashed lines), horizontal convergence (thin solid lines), twisting (thick solid lines), diffusion effect (dotted lines), and the sum or net effect (open circles with dots).

in balance with the pressure field through the gradient wind relation, has no explicit dynamical instability for the growth of a radial-vertical circulation, since the baroclinicity is too weak to overcome the inertial stability. It should be also noted here that the initial stratification is statically stable but conditionally unstable everywhere.

Starting from the above-mentioned initial state, a very weak radial-vertical circulation is established within several hours. In the earlier period, the azimuthal momentum v is decreased from below by the vertical diffusion process. Thus, the gradient wind balance is destroyed and the inward acceleration of the air developes starting from below. As time goes on, a quasi-balance among the Coriolis force, the pressure gradient force and the frictional force is attained. The role of the inertia force is negligible at this early stage. In the boundary layer, the inflow is maximum at the lowest level and decreases with height, while v increases with height.

The inflow in the boundary layer is accompanied by upward vertical motion in the troposphere and outflow below the tropopause. It will be shown in the next section that the radial flow, when integrated vertically, does not give rise to a mass shift except during the deepening stage. Anyway, the vertical shear of the radial flow (i.e., $\partial u/\partial z$) is positive in most parts of the troposphere. This continues to be a main characteristic of the radial flow even when the radial-vertical motion becomes subject to other factors besides the boundary layer processes. Accordingly, the evolution of the radial-vertical circulation is investigated through the analysis of the time rate of change of $\partial u/\partial z$.

The equation for $\partial u/\partial z$ is written as

$$\frac{\partial}{\partial t}\frac{\partial u}{\partial z} = BA + BB + BC + BD \qquad (11.1)$$

where:

BA   the advective term $[= (\partial/\partial z)$ (large-scale advection of u)$]$

BB   the moment due to the Coriolis (radial component) and centrifugal forces $[= (\partial/\partial z)(fv+v^2/x)]$

BC   the solenoidal field on the x-z plane $[= (\partial/\partial z)(-\partial\phi_p/\partial x)]$

BD   the contribution of frictional force F_u $\{= (\partial/\partial z)[(_HF_u+_VF_u)/p_*]\}$.

The term BC represents the baroclinicity vector in the present model, since it contains only the azimuthal component.

Once the vertical flow is organized in the conditionally unstable atmosphere through (in the present case) boundary layer processes, a warm core may develop. As discussed in Section 7, a warm core is formed through a delicate imbalance between the cooling due to large-scale motion and the warming due to the condensation-convection process. The warm core formation is implied by the increase of term BC, which plays an active role in the further development of radial-vertical flow.

Fig. 30 shows the distribution of BC for the periods P2, D1, D2 and M1. The buildup of BC, especially during the deepening stage, is achieved through a positive feedback process. When BC increases, the inflow and, subsequently, the azimuthal wind in the lower free atmosphere intensify. Then the term BB becomes large in the boundary layer and the inflow near the surface becomes stronger. The intensified inflow as well as the supply of latent energy from the ocean to the air subsiding into the boundary layer in the outer area contribute to the further development of the solenoidal field BC.

As shown in Fig. 30, an area of large positive BC approaches the center in the deepening stage. This movement coincides with the shrinking of the vortex. The height of maximum BC changes from the 400-mb level for period P2 to 250 mb at M1. In the deepening stage, an area of negative BC appears in the upper troposphere near the center. This is favorable for establishing the downward motion at the center. This negative area disappears in period M1. Another negative area is seen at around 100 km radius at low levels, suggesting a slightly cooler area near the center. However, in the equation for $\partial u/\partial z$, the contribution by BC in the boundary layer is very small compared with that of the other terms. A third area with negative BC develops at about the 200-mb level outside a large positive region after period D2. This may be related to a secondary circulation to be discussed later.

After the period M1, the maximum BC decreases gradually. This is consistent with a broadening of the warm core and hence a decrease in the horizontal contrast of temperature. At the period M3, the maximum value is 492×10^{-8} s^{-2}. A small area of negative BC located at the center lower levels at M1 develops vertically later. It reaches to the 350-mb level at M3.

The other terms (BA, BB, BD) were also investigated. Based on the results of these analyses, it may be concluded that the evolution of $\partial u/\partial z$, which manifests in the development of the wind field as presented in Figs. 8–10, primarily results from a delicate imbalance between the self-amplified term BC and the counter term BB in the free atmosphere and further from a difference between the rather passive term BB and the term BD in the boundary layer.

b. Control of radial-vertical circulation

At the end of the deepening stage, when the conditional instability disappears near the center and the term BC attains its maximum intensity, a quasi-balanced state is achieved among the terms in the $\partial u/\partial z$ equation, and the acceleration of $\partial u/\partial z$ ceases.
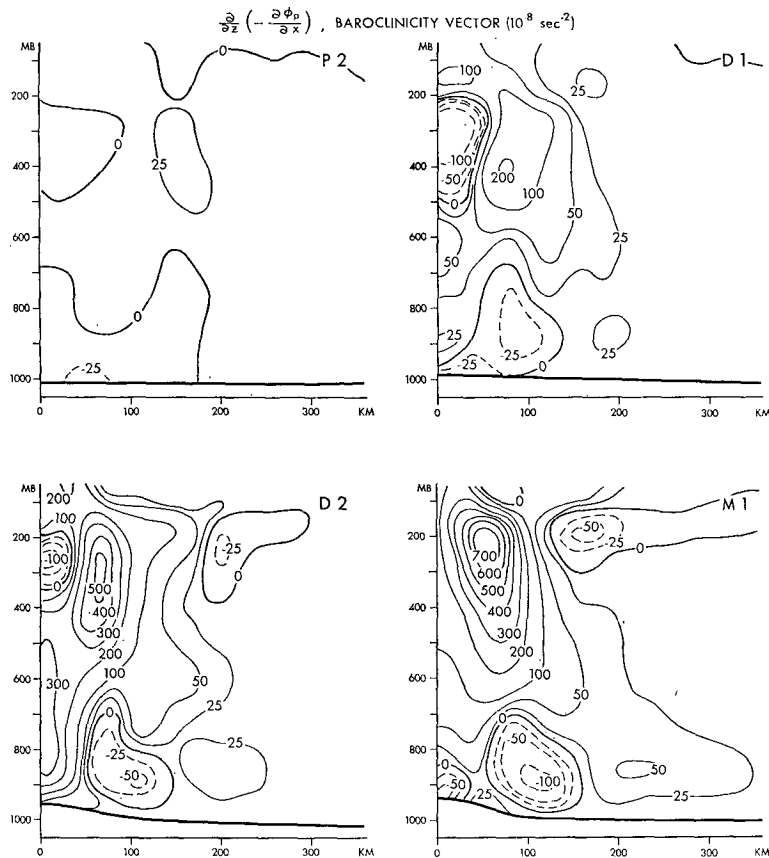
FIG. 30. Vertical cross sections of baroclinicity vector (10^{-8} s^{-2})
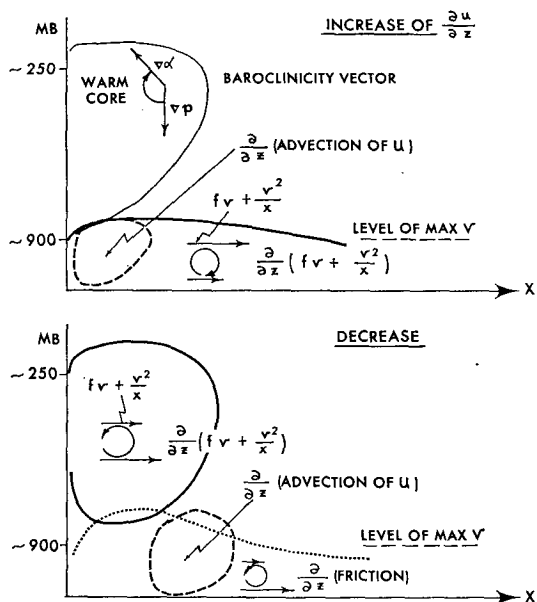for periods P2, D1, D2 and M1.

FIG. 31. The radial-vertical distribution of the factors which contribute to the increase of $\partial u/\partial z$ (upper figure) and to the decrease (lower figure) at the mature stage. The terms BA, BB, BC and BD in Eq. (11.1) are indicated by dashed, thick solid, thin solid and dotted lines, respectively.

The distributions of the factors which contribute to the increase of $\partial u/\partial z$ and those to its decrease are shown schematically in Fig. 31.

As mentioned earlier, the term BC in the free atmosphere and the term BB below the level of maximum v contribute positively. Near the center at the lower levels, BA also acts to increase $\partial u/\partial z$. The counterbalancing term is shown in the lower part of the figure. Above the level of maximum v, the Coriolis and the centrifugal forces decrease with height to make the term BB counteract the solenoidal acceleration BC. In the boundary layer, the frictional effect BD is a dominant negative term, while at a certain radius, BA also gives a negative contribution.

The vertical distribution of the terms in the $\partial u/\partial z$ equation at 60 km radius for the period M1 is shown in Fig. 32. In the free atmosphere, BC is balanced by BA+BB. Below the level of maximum v, a balance is maintained between BB and BA+BD.

c. Development of secondary circulation

In the course of the development of the storm, the vertical component of relative vorticity in the upper outer area decreases by the effects of horizontal di-
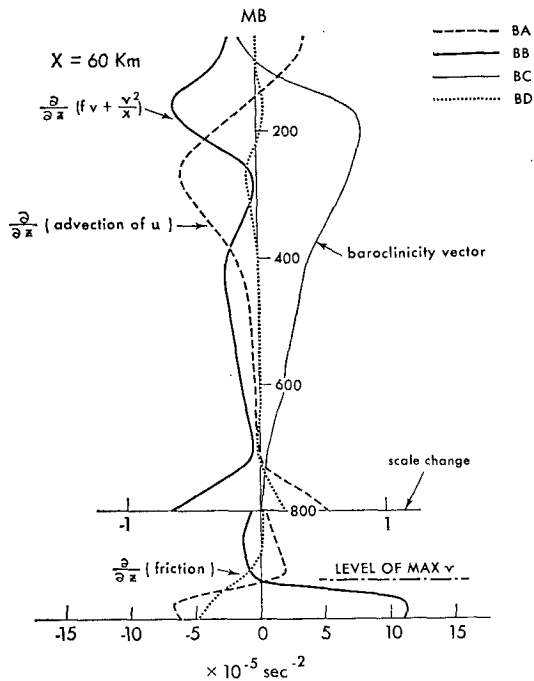
FIG. 32. Vertical distribution of budget components in the equation for $\partial u/\partial z$ [(11.1)] at 60 km radius for period M1.

vergence and twisting (see Figs. 27 and 28). Eventually, these processes produce a negative absolute vorticity η [$=f+\zeta$] in certain regions (Fig. 25). The inertial stability of a circular vortex is measured by $\xi\eta$, where $\xi=f+(2v/x)$ (e.g., Yanai, 1964). Accordingly, the appearance of an area with negative η or negative ξ (i.e., anomalous wind) is a favorable factor for the growth of a symmetric radial-vertical circulation. On the other hand, the system is statically stable, i.e., the static stability S [$=g\partial \ln\theta/\partial z$] is positive. Because of this, the circulation, if it develops, will show a flattened pattern.

In the case of a baroclinic circular vortex, the baroclinicity B, which is defined as $\partial(-\partial \phi_p/\partial x)/\partial z$, may contribute to the development of a radial-vertical circulation. This problem has been studied by many investigators [see, e.g., the review paper by Yanai (1964); and the articles by Ooyama (1966) and McIntyre (1970)]. For an adiabatic inviscid fluid, the necessary criterion for the development of radial-vertical circulation is that $\xi\eta S - B^2 < 0$ is met at least in a part of the domain. This criterion means baroclinic instability along a constant absolute angular momentum surface, or inertial instability along an isentropic surface (e.g., Yanai, 1964).

It was mentioned earlier that the initial field in the present experiment was dynamically stable since the baroclinicity B was very small and $\xi\eta>0$. As the integration proceeds, the warm core intensifies and hence B becomes large. In addition, the absolute vorticity decreases in a certain region and even be-

comes negative. Accordingly, the criterion $\xi\eta S - B^2 < 0$ may be met somewhere in the domain. In Fig. 33, the solid lines show the distribution of this quantity for the period M1. It is clear that instability may occur in the outer area of the storm, particularly at the upper levels. The contours of $\xi\eta S - B^2 = 0$ for D1 and D2 are also shown in the figure by dotted and dashed lines, respectively. An expansion of the unstable region is seen. The first appearance of a small negative area was noticeable at P3. The cross mark and the attached number in the figure indicate the most unstable position and the value of the instability parameter at that position for D1, D2 and M1, respectively.

Following Ooyama's study (1966), Yanai and Tokioka (1969) performed a numerical experiment and showed that, if the above-mentioned instability is met in a part of the domain, the development of a radial-vertical motion is confined within that domain. The evolution of the secondary circulation in the present model agrees with theirs. Namely, it develops, as shown in Figs. 9 and 10, in the upper outer region of the storm where one would expect the instability to occur according to Fig. 33. It seems that such a secondary circulation affects the budget of the various quantities only locally and thus has little effect on the intensity or any other major characteristic of the tropical cyclone. A similar conclusion was reached in the numerical experiment by Yamasaki (1968b).

The appearance of negative absolute vorticity is related to the secondary circulation in the present model. It may also contribute to the evolution of
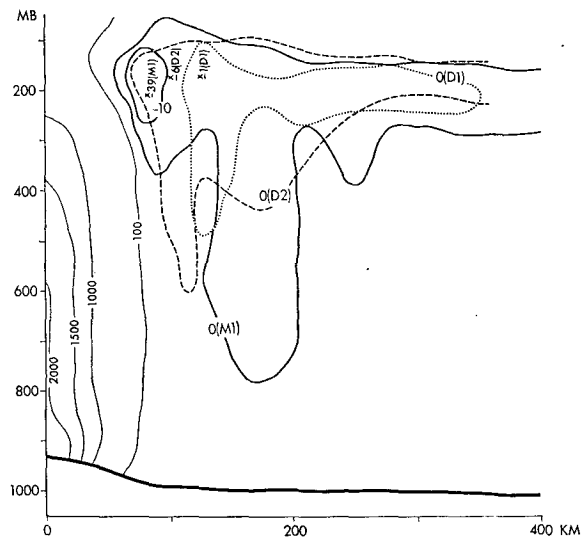

FIG. 33. Vertical cross section of the instability parameter $\xi\eta S - B^2$ (all units 10^{-12} s^{-4}) for period M1 (solid line). Zero isopleths for periods D1 and D2 are also shown by the dotted and dashed lines, respectively. The cross marks and the attached numbers indicate the most unstable positions and the values of the parameter for periods D1, D2 and M1.
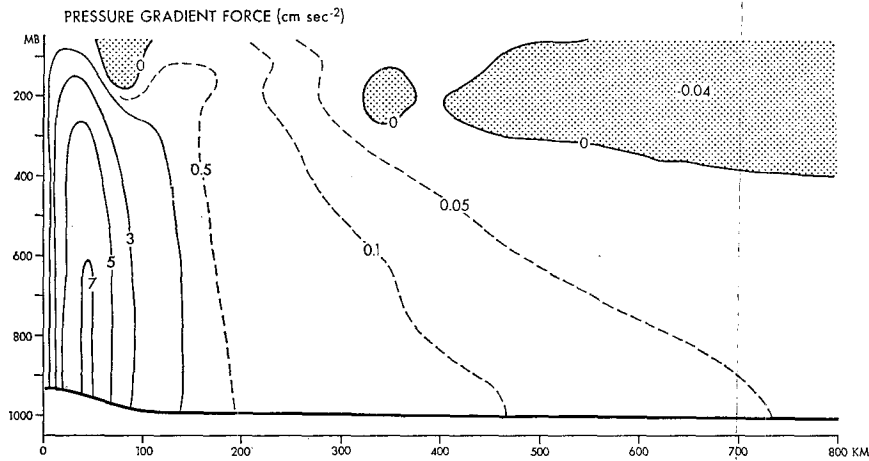
PRESSURE GRADIENT FORCE (cm sec^{-2})

FIG. 34. Vertical cross section of pressure gradient force for period M1.
Areas with negative value are shaded.

axially asymmetric motion if the model is three-dimensional (e.g., Anthes, 1972). The existence of a basic flow may change or modify the feature of the secondary circulation discussed in this subsection.

12. Pressure field and balance of forces

a. Pressure field

The distribution of the horizontal pressure gradient force during period M1 is presented in Fig. 34. Inside

100 km, this force is about 100 times larger than that at about 600 km. The maximum gradient is seen at about 40 km. The zero isopleth in the figure indicates the position of a pressure ridge. It extends nearly horizontally to the 450-mb level at the lateral boundary.

Very low pressure near the center, of course, results from the net outflow of mass from the central region during the deepening stage. In Fig. 35, the mass fluxes across the 100 km radius above and below the level $\sigma = 0.86$ are shown respectively by curves A and B. A positive value (in arbitrary units) implies
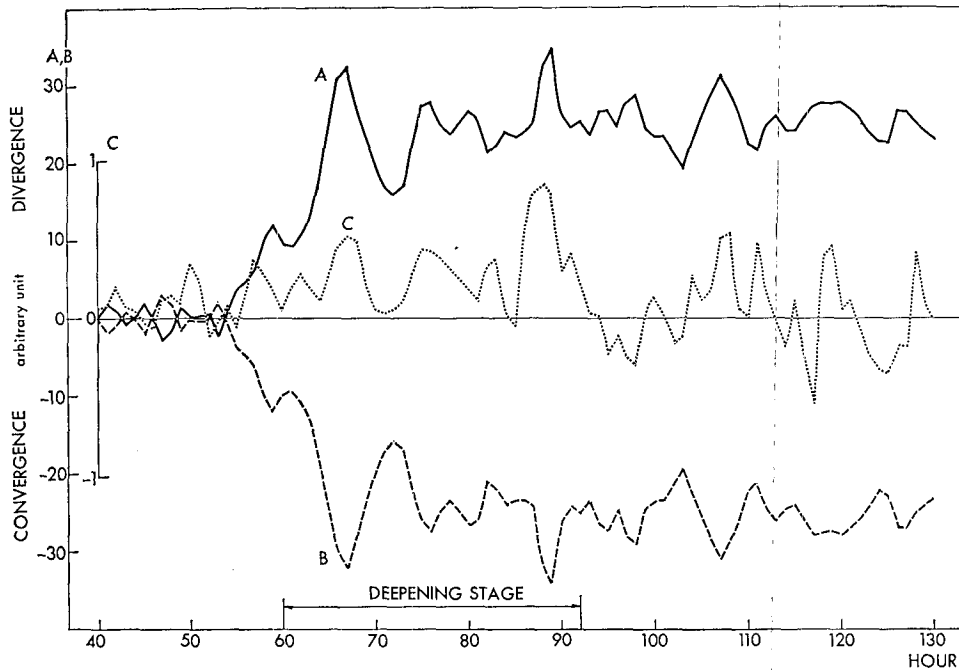
FIG. 35. Time series of mass fluxes across the 100 km radius above the level $\sigma = 0.86$ (solid line A) and below that level (dashed line B). Dotted line C shows the net flux, i.e., A+B. Scale for C is magnified 20 times as compared with those for A and B.
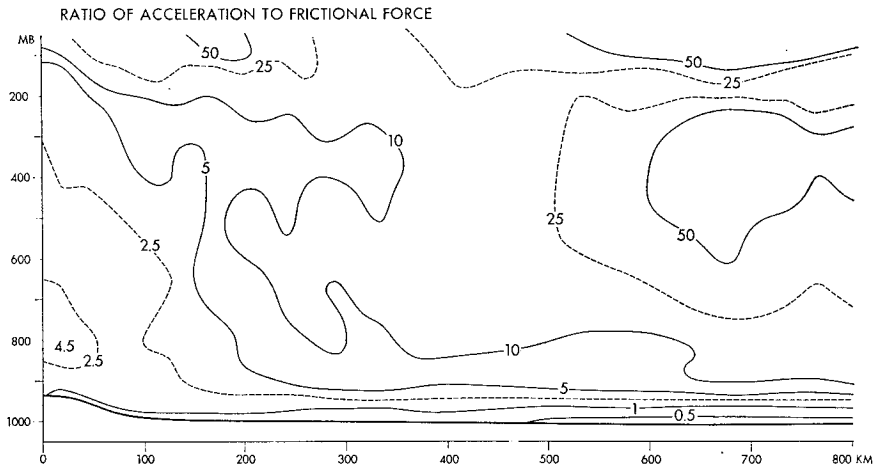
RATIO OF ACCELERATION TO FRICTIONAL FORCE

Fig. 36. Vertical cross section of the ratio of inertia acceleration to frictional force
(the Reynolds number) at period M1.

mass export from the central area and a negative value implies mass import. In the figure the net mass flux (i.e., A+B) is shown by curve C on a magnified scale (20 times). In general, A and B are negatively correlated and the sum C is very small. The figure shows that the curve C is shifted to the positive side, which means net outflow of mass, during the deepening stage. One may speculate that the acceleration of low-level inflow in this period is slightly smaller than that of upper level outflow perhaps because of boundary layer processes. At the predeepening and the mature stages, the net flux C fluctuates around a value of zero so that the trend of surface pressure is small.

b. Balance of forces

In order to investigate a state of balance among various forces in the mature stage, some of the ratios between the forces for period M1 are estimated. The

forces are defined as follows:

Acceleration or inertia force
$$= \{[-\mathbf{v} \cdot \nabla u - \dot{\sigma}(\partial u/\partial \sigma)]^2 + [-\mathbf{v} \cdot \nabla v - \dot{\sigma}(\partial v/\partial \sigma)]^2\}^{\frac{1}{2}}$$

Coriolis force (including centrifugal force)
$$= |f + (v/x)| (u^2 + v^2)^{\frac{1}{2}}$$

Frictional force
$$= (1/p_*)[(_\mathrm{H}F_u + _\mathrm{V}F_u)^2 + (_\mathrm{H}F_v + _\mathrm{V}F_v)^2]^{\frac{1}{2}}.$$

The spatial distribution of the ratio between the acceleration and frictional force, which may be referred to as the Reynolds number (Re) is shown in Fig. 36, while the one between the acceleration and Coriolis force, which may be called the Rossby number (Ro) is presented in Fig. 37.

Fig. 36 shows that Re is greater than 5 except for the storm region and the planetary boundary layer. In other words, the frictional effect is negligible in a
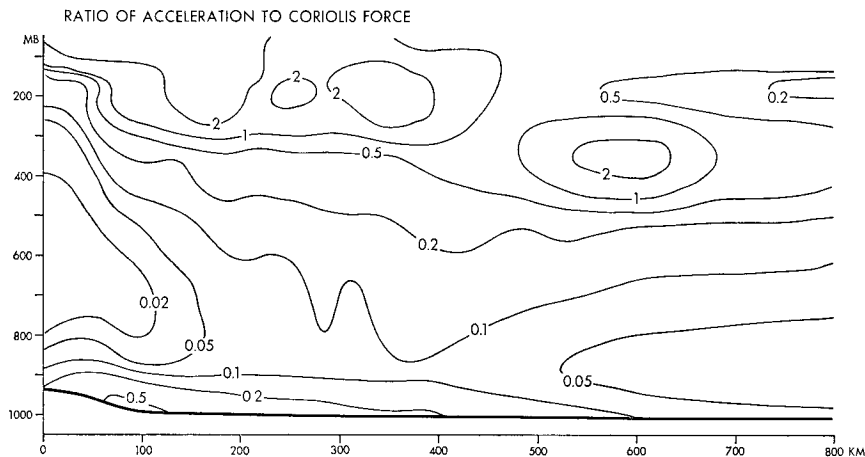
RATIO OF ACCELERATION TO CORIOLIS FORCE

Fig. 37. Vertical cross section of the ratio of inertia acceleration to Coriolis plus
centrifugal force (the Rossby number) at period M1.

large part of the domain, especially at the middle level beyond 500 km and in the stratosphere. It is interesting to note that a thin layer of relatively small Re exists at 200 mb beyond 500 km. Near the surface, Re is smaller than 1 but it is larger than 0.5 inside the 450 km radius. This means that the inertia force is important in discussing the balance of forces in the inner region of the boundary layer. This fact was pointed out before by Ogura (1964) and Ooyama (1969a, b).

The ratio of inertia force to Coriolis force, including centrifugal force, is smaller than 1 in most parts of the domain. The exception is the upper levels inside 700 km as shown in Fig. 37. A large value of Ro in a region of large Re implies either that a balance of forces is mainly between the inertia force and pressure gradient force or that the Coriolis and centrifugal forces nearly cancel each other in a certain domain of anticyclonic flow. Fairly good gradient wind balance may be observed in the middle and lower free atmosphere where Ro is small and Re is large. Possible importance of inertia forces in the inner area of the boundary layer is again shown by a slightly larger value of Ro.

A detailed analysis of the radial acceleration at levels 2, 5 and 11 for period M1 follows. The equation for the radial momentum is written as

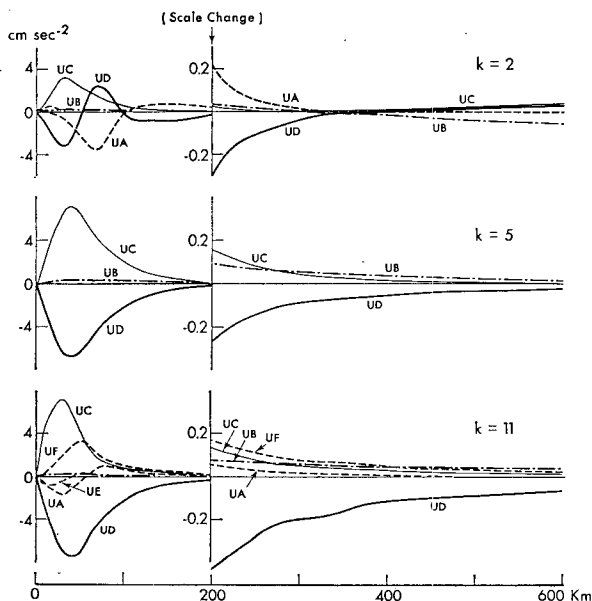$$\frac{\partial u}{\partial t} = UA + UB + UC + UD + UE + UF,$$

Fig. 38. Radial distribution of the radial acceleration due to inertia term (UA, dashed line), Coriolis force (UB, dash-dotted line), centrifugal force (UC, thin solid line), pressure gradient force (UD, thick solid line), horizontal diffusion effect (UE, dashed line) and vertical diffusion effect (UF, dashed line) at the levels 2, 5 and 11 at period M1.

where:

UA   inertia term or advection of u
UB   Coriolis force $[=fv]$
UC   centrifugal force $[=v^2/x]$
UD   pressure gradient force
UE   effect of horizontal diffusion
UF   effect of vertical diffusion.

The gradient wind balance is the balance between UB+UC and UD for cyclonic flow and between UB and UC+UD for anticyclonic flow. Such a balance may be modified by other terms which can effectively increase or decrease the effect of UD, so that the wind becomes supergradient or subgradient.

The radial distributions of each force are shown in Fig. 38. At level 2 ($\sim$120 mb), the wind near the center is approximately cyclostrophic, i.e., the balance is between UC and UD. Between 50 and 100 km, the Coriolis and centrifugal forces are in the direction of the pressure gradient force. The sum of these forces (UB+UC+UD) is balanced by UA. Both UB and UC become small between the 100 and 300 km. The main balance there is between UD and UA. Outside the pressure ridge, which is located at around 350 km, the wind is anticyclonic gradient, i.e., the balance is between UB and UC+UD. The term UA is not important there.

At the middle level, $k=5$, the azimuthal flow is almost cyclostrophic within 150 km radius and is gradient beyond that radius. The terms UA, UE and UF are all negligible.

At the lowest level, $k=11$, the main feature is characterized by a state of balance for the Ekman layer of a cyclonic flow, i.e., UB+UC+UF vs UD. However, the inward accelerating force in the present case is augmented by the inertia force UA within 60 km and is diminished by UA between 60 and 400 km. Accordingly, the balance condition requires a stronger wind in the former area and a weaker wind in the latter area, respectively, than the wind which may be expected for a simple Ekman layer.

The balance of forces in the azimuthal direction was investigated in Section 9 from the viewpoint of angular momentum balance.

13. Energy budget analysis

a. General feature of the energy budget

The mean amount of energy in different forms for the whole system at each period is given in Table 5. These figures are obtained from a time average of the area mean of $\int_0^1 E p_* d\sigma / g$, where E may be either Lr (latent energy), $c_v T$ (internal energy), gz (potential energy) or $\frac{1}{2}(u^2 + v^2)$ (kinetic energy).

The internal plus potential energy, or the total potential energy, increased over the periods from P1 to M3 by 27 (units 10^9 ergs cm^{-2}). The kinetic energy

TABLE 5. Mean energy content (10^9 ergs cm^{-2}) for the total domain and for the area within the 500 km radius. Mean mass, in terms of mean surface pressure, is also listed.

| Period | Total domain | | | | Within 500 km radius | | | |
	Latent	Internal plus potential	Kinetic	Mass (mb)	Latent	Internal plus potential	Kinetic	Mass (mb)
P1	126.4	2689.4	0.01	1009.4	129.7	2686.9	0.10	1007.5
P2	125.5	2691.1	0.02	1009.4	131.4	2688.2	0.22	1006.7
P3	124.2	2693.3	0.05	1009.4	128.5	2689.3	0.45	1005.7
D1	122.8	2695.4	0.09	1009.4	122.9	2689.7	0.77	1004.6
D2	121.9	2696.9	0.12	1009.4	118.8	2689.7	1.08	1003.4
M1	119.5	2700.6	0.16	1009.4	116.2	2692.3	1.37	1002.3
M2	113.2	2709.7	0.25	1009.4	109.0	2699.8	1.59	1000.3
M3	108.7	2716.4	0.31	1009.4	109.4	2706.9	1.50	1000.3
Change from P1 to M3	−17.8	+27.0	+0.30	0.0	−20.4	+20.0	+1.41	−7.2

also increased by 0.3 unit. This increase is obviously due to the excess of generation over the dissipation of kinetic energy. On the other hand, the latent energy at M3 is smaller than that at P1 by 17.8 units. The increase in total energy is 9.5 units. Since the present system is energetically insulated at its lateral boundary and the frictional dissipation is not included in the net heating in the present model, $(9.5+\epsilon)$ units of energy, where ϵ is the dissipated kinetic energy, have been supplied to the system across the bottom boundary.

Next, the transport of energy across a hypothetical cylindrical vertical wall at various radii will be examined. This transport is equal to $\int_0^1 2\pi x E u p_* d\sigma/g$. If p/ρ is substituted for E, the formula gives the pressure work across the wall which is comparable with an energy transport. Fig. 39 shows the radial distribution of the vertically integrated energy transport estimated at period M1. A positive flux means an outward transport.

Both internal and latent energy are transported inward at any radius. The transport increases as the radius becomes smaller, down to 150 km. This implies that the outer area of a storm is an effective source region of these two forms of energy. The pressure work acts in the same sense as the flux of internal energy. Because the circumference of a cylindrical wall is proportional to radius, the energy flux per unit azimuthal length changes rapidly with radius. Within 150 km radius, there exists a tremendous convergence of internal and latent energy. On the other hand, the divergence of potential energy from the same area is equally large. The overall energy balance near the center is quasi-stationary at the mature stage. Therefore, a strong conversion among the different forms of energy must take place in this region. The transport of kinetic energy is two orders of magnitude smaller than that of the other forms of energy. Its distribution indicates convergence into a small central area and the divergence outside of it.
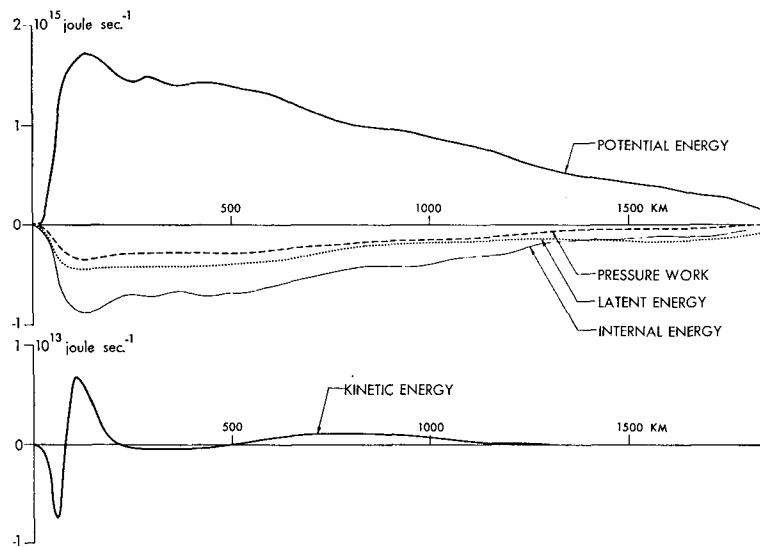

FIG. 39. Radial distribution of energy transport across the cylindrical vertical wall at period M1. An outward transport is expressed as a positive flux.
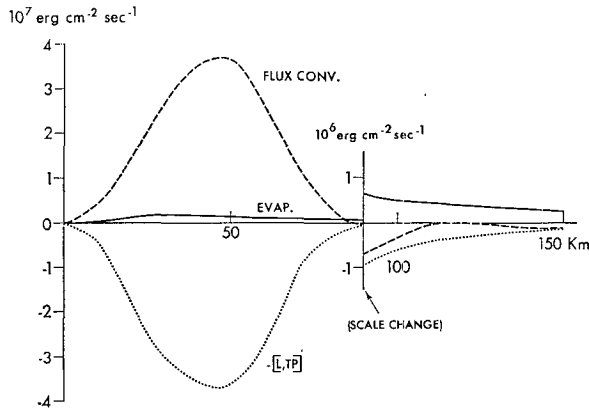
10^7 erg cm^{-2} sec^{-1}

FIG. 40. Radial distribution of the vertical integrals of the latent energy budget components at the period M1: changes due to latent heat flux convergence (dashed line), evaporation (solid line), and the conversion to the total potential energy (dotted line). Changes due to horizontal diffusion are too small to plot.

In Table 5, the energy statistics within 500 km radius is also shown. The energy budget for such a subdomain cannot be discussed without considering the above-mentioned energy transport across the open boundary of the subdomain. In fact, the time variations of latent and total potential energy as seen in the table result from small differences between very large energy transports and energy conversions. According to Fig. 39, only the transport of kinetic energy decreases sharply in the outer area. The kinetic energy is nearly self-contained, at least after taking the vertical integral, in the region within 500 km.

b. Budget of latent energy

The budget of moisture (i.e., latent energy) was discussed in detail in Section 8. Here, the budget for an air column at different radii in period M1 is presented in Fig. 40. The horizontal flux convergence is a major source of latent energy within the 80 km radius, while the relative importance of evaporation as a local energy source becomes large beyond 100 km. The dotted line in the figure, which is labeled as —[L,TP], represents the loss of latent energy by the condensation process. Through the release of latent heat of condensation, the latent energy is transformed into the total potential energy. The supply and the conversion of latent energy in the inner area are balanced so well that the residual is practically zero.

As discussed by Ooyama (1969a), and revealed by the analysis in Section 8, the evaporation in the outer area supplies the latent energy to the subsiding air and eventually contributes to the large flux convergence of latent energy into the inner area. However, as can be inferred from Ooyama's discussion, such large flux convergence is possible only in the presence of evaporation in the inner area, although evaporation appears to be negligible in the water budget as seen

in Fig. 40. If the evaporation in the inner area is suppressed at the mature stage, the equivalent potential temperature of the inflowing low-level air cannot be raised. Accordingly, the already established warm core starts to weaken. Then, the radial-vertical circulation is decelerated and flux convergence of latent energy is reduced. This, in turn, causes further weakening of the warm core and a decrease of convergence of latent energy. In this way, a tropical cyclone loses its intensity. An extra experiment was performed to support the above argument. Here we note that, in the present (control) model, the central surface pressure and the maximum wind at the lowest level were 934.0 mb and 60.6 m s^{-1}, respectively, at Hour 120, and 942.6 and 53.9 at Hour 144. In the extra experiment, the evaporation inside 200 km, which was quite small in the control experiment as compared to the moisture influx into that region, was suppressed to zero after Hour 120. At that time the above-mentioned quantities at Hour 144 changed to 969.3 mb and 37.4 m sec^{-1}, respectively, indicating the weakening of a tropical cyclone.

c. Budget of total potential energy

The budget of heat was analyzed in Section 7. If each term of (7.1) is multiplied by c_p and the vertical mass integral is taken, then, after some manipulation, the equation for total potential energy of an air column is obtained in a so-called flux form. In particular, the term TB in (7.1) multiplied by c_p may be divided into two terms, one representing the in situ transformation of total potential energy into kinetic energy, which may be denoted by —[TP,K], and the other expressing the effect of energy redistribution. The term TE yields the conversion of latent energy to total potential energy, i.e., [L,TP]. The
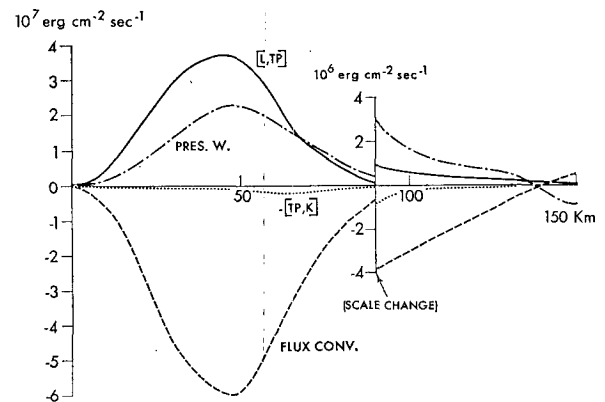
10^7 erg cm^{-2} sec^{-1}

FIG. 41. Radial distribution of the vertical integrals of the components in the total potential energy budget for period M1: changes due to flux convergence (dashed line), pressure work (dash-dotted line), conversion from the latent energy (solid line), and conversion to the kinetic energy (dotted line). The effect of diffusion is too small to plot.
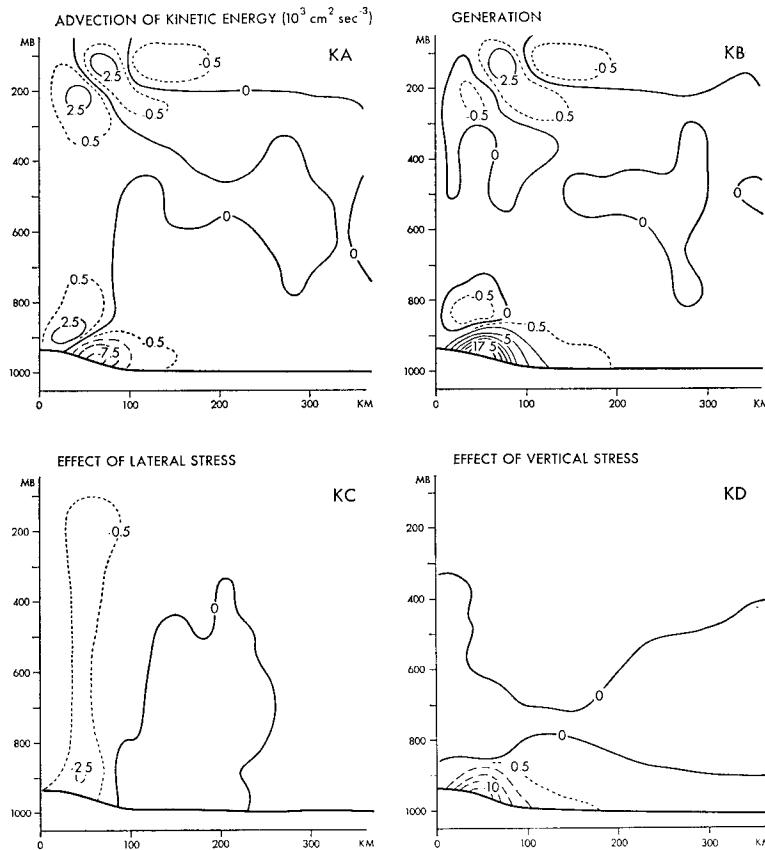
FIG. 42. Vertical cross sections of kinetic energy budget components at the period M1: changes (all units 10^3 cm^2 s^{-3}) due to advection (KA), generation (KB), and effects of lateral stress (KC), and vertical stress (KD).

remaining terms are the convergence of enthalpy and the diffusion effects.

The radial distribution of these terms at the period M1 is shown in Fig. 41. The diffusion effect is too small to plot. The figure shows that, within 150 km radius, the energy conversion term [L,TP] is almost balanced with the sum of the flux terms including the pressure work. Since the flux convergence of internal energy and the pressure work term have the same sign, the present result implies that an enormous export of potential energy to the outer area does take place (see Fig. 39).

The conversion of total potential energy to kinetic energy, i.e., [TP,K], is only a very small fraction of the conversion from latent to total potential energy, [L,TP]. In other words, the heat which is utilized to maintain the motion field is only a tiny portion of the total heat released by the condensation of the water vapor. The ratio of the area integral of [TP,K] to that of [L,TP] gives a measure of the efficiency of the heat engine of the system as a whole. It varies from 1-2.4% at the pre-deepening stage, increases through the deepening stage, reaches 7.7% at M1, and then gradually decreases to 6.7% at M3. The

observed estimate of efficiency by Palmén and Riehl (1957) is 3%.

d. Budget of kinetic energy

The equation for the local change of kinetic energy $K[=\frac{1}{2}(u^2+v^2)]$ is easily derived from the momentum equation. It takes the form

$$\frac{\partial K}{\partial t} = KA + KB + KC + KD$$

where:

KA   advection of K
KB   generation of kinetic energy $[= -u(\partial\phi_p/\partial x)]$
KC   change of K due to lateral stresses.
KD   change of K due to vertical stresses.

Both terms KC and KD consist of two parts, namely, the internal dissipation of kinetic energy and the work done by stresses. The stress at the bottom boundary leads to the frictional dissipation of energy at the air-sea interface.

Fig. 42 shows the spatial distribution of each of the above terms at period M1. The term KB is large
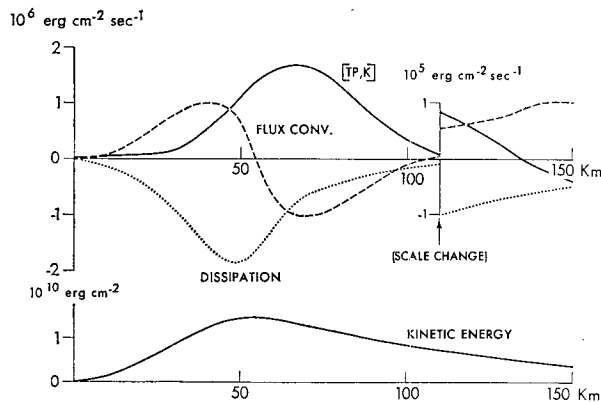
FIG. 43. Radial distribution of the vertical integrals of the kinetic energy budget components at the period M1: changes due to flux convergence (dashed line), conversion from the total potential energy (solid line), and dissipation (dotted line). Radial distribution of kinetic energy in an air column is shown in the lower part.

positive in the boundary layer near the center. This is caused by the strong inflow down the pressure gradient. Areas of negative KB are associated with outflow in the region where pressure increases outward.

It is seen in the figure that KA is negatively correlated with KB. This means that kinetic energy is advected from the place where it is generated to the place where it is converted into total potential energy. In the boundary layer, especially in an inner area, KA+KB is positive. This is balanced primarily by KD. The term KC seems to be significant in the balance of K in the free atmosphere. A weak positive KC apparently results from the momentum acceleration due to the lateral stress.

The budget of kinetic energy for a vertical air column may be examined by taking the vertical mass integral of the kinetic energy equation. The result is shown in Fig 43, together with the radial distribution of kinetic energy in an air column. The integral of KB is equivalent to [TP,K]. This is positive and large inside 100 km; that is, the radial flow and the radial gradient of pressure are negatively correlated in an air column. Since the primary feature of radial flow is the low-level inflow and the upper-level outflow, it follows that, as stated by Palmén and Riehl (1957), the existence of a warm core, or the upward motion in it, is a condition for kinetic energy generation. It is of interest to note that the peak in [TP,K] is located about 20 km outside of the place of maximum [L,TP].

The vertical integrals of KC and KD are combined to draw a dotted line labeled as dissipation in the figure. The maximum dissipation is located at the radius where [L,TP] is largest rather than where [TP,K] is maximum. This position coincides with the place where kinetic energy is largest. The dissipation exceeds the generation within the 60 km radius and

the reverse is true outside of it. This agrees with the results obtained by Palmén and Riehl (1957) for a mean tropical cyclone and by Ooyama (1969a) in his numerical simulation experiment. Thus, an inward transport of the kinetic energy is required for the maintenance of the kinetic energy in the inner region. The dashed curve in Fig. 43 reflects such a transport of kinetic energy.

e. Energy budget within the 500 km radius

The energy budget within 500 km is summarized in Table 6. The main processes are low-level inflow of Lr and addition of latent energy through evaporation at the surface, transformation of Lr to $c_vT+\phi$, import of c_vT and increase of energy due to work done by the pressure force, upper level outflow of ϕ^ι transformation of total potential energy to K, and dissipation of K due to lateral and surface stresses.

According to an estimate by Palmén and Jordan (1955), the production of kinetic energy within a 6° radius of the mean hurricane is 1.1×10^4 ergs cm^{-2} s^{-1}. The generation rate in the present model is almost four times larger. The estimate of dissipation due to ground friction by Palmén and Riehl (1957) is 0.9×10^4 ergs cm^{-2} s^{-1}, i.e., about 60% of the value in the present model.

14. Summary and remarks

A tropical cyclone was successfully simulated in a numerical model. The major structural features of tropical cyclones were obtained despite the simplicity of the model, i.e., the assumed axisymmetry of the disturbance, an insulated lateral boundary, and lack of radiational effect.

Detailed budget analyses of the important meteorological variables, such as temperature, moisture, rela-

TABLE 6. Energy budget for the domain of 500 km radius at period M1.

| Energy (10⁹ ergs cm⁻²)	Convergence and transformation (10⁴ ergs cm⁻² s⁻¹)	
Latent energy (Lr) 116.15	Flux convergence of Lr	49.369
	Effect of horizontal diffusion	0.046
	Evaporation at the surface	13.012
	Conversion to $c_vT+\phi$	−60.260
Total potential energy ($c_vT+\phi$) 2692.3	Conversion from Lr	60.260
	Flux convergence of c_vT	86.846
	Flux convergence of ϕ	−180.445
	Effect of pressure work	34.739
	Effect of horizontal diffusion	−0.100
	Sensible heat flux at the surface	−0.961
	Conversion to K	−4.177
Kinetic energy (K) 1.366	Conversion from $c_vT+\phi$	4.177
	Flux convergence of K	0.001
	Effect of lateral stress	−1.785
	Internal dissipation due to vertical stress	−0.619
	Dissipation due to surface stress	−1.546
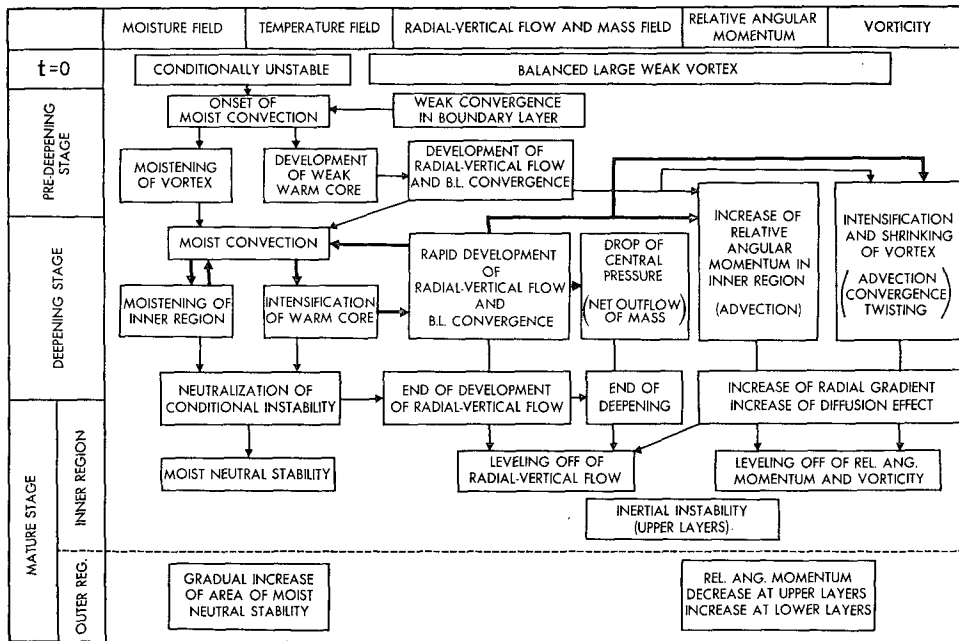
Fig. 44. Summary diagram of the results of the analysis.

tive angular momentum, vorticity, radial-vertical circulation and kinetic energy, were performed in order to study the evolution of a tropical cyclone in the model.

Fig. 44 summarizes the principal results of the present analysis. The sequence of events shown is explained in the following. As initial conditions, a balanced weak vortex is given in a conditionally unstable atmosphere. Gradually, the radial flow starts to develop in the boundary layer through the diffusion process. This is accompanied by the development of a vertical motion field, which is upward and relatively large where vorticity is large. Adiabatic cooling in the region of upward motion is more than offset by the effect of moist convection. Thus, a solenoidal field is formed which accelerates the motion field that is favorable for an intensification of the moist convection. Whether the solenoidal field is established or not at the pre-deepening period is determined by a delicate heat budget which depends on the static stability of the free atmosphere and the moisture content in the boundary layer. In this respect, sea surface temperature is an important parameter.

The processes which involve the deepening of a tropical cyclone are linked by the thick arrows in Fig. 44. Especially important is a positive feedback process which builds up a warm moist core, accelerates the radial-vertical circulation, and intensifies moist convection. The increase in the generation of kinetic energy is in accordance with this process. The net outflow of mass from the central region takes place during this period and the central surface pressure

drops sharply. The vertically integrated relative angular momentum in the inner area increases largely through the net import of relative angular momentum. The vorticity at the inner side of the vortex ring increases by the effects of advection, horizontal convergence and twisting. This causes an intensification and shrinking of the vortex.

The deepening stage ends with neutralization of the conditional instability in the central region. The acceleration of the radial-vertical circulation ceases since the baroclinicity vector in the free atmosphere is counterbalanced by the moment of the Coriolis plus centrifugal forces. By this time, both relative angular momentum and vorticity concentrate near the center and the role of vertical diffusion as well as that of horizontal diffusion in the budget equations become significant. It is interesting that not only the radial-vertical circulation, but also the relative angular momentum and relative vorticity in the inner area level off at the time when moist neutral stability is reached. In the troposphere, except the upper part and the boundary layer, the azimuthal flow and the pressure field satisfy the gradient wind relationship. In the boundary layer, a simple Ekman flow is modified by the inertia acceleration.

As a result of the development of a warm core and the decrease of vorticity outside the storm, inertial instability along the isentropic surface may occur at the upper levels in the outer region. This causes a secondary radial-vertical circulation in a limited domain. It seems that this circulation does not alter the main characteristics of the tropical cyclone.

At the mature stage, the status in the inner region is quasi-stationary. For the maintenance of kinetic energy, the transport process and the generation are equally important. On the other hand, the status in the outer region keeps changing slowly; that is, the area of moist neutral stability is expanded and the relative angular momentum increases at the lower levels while it decreases at the upper levels.

The broad-scale features of a tropical cyclone, particularly those at the mature stage, are well revealed by the budget analyses described in the present paper. It has to be noted, however, that the local balance among various components in the budget equations is still not quite conclusive. Assume, for example, that the formula used to estimate the stress in the momentum equations is changed. Then, a new state of local balance will be obtained among the components, the magnitude of which may be different, hopefully not drastically, from the present results.

In the present analysis, a time average is taken for a period ranging from 11 to 21 h in order to show a mean status for each period. One of the modes which are obscured through such a process is an outward propagating wave with the period 3–5 h. Its amplitude is small and the coupling of this wave with the mean field or its contribution to the budget of the mean field seems to be very small. The structure of this wave is quite similar to that of the spiral bands which appeared in a three-dimensional numerical model (Kurihara and Tuleya, 1974). It is probable that a spiral band takes a distorted form in the present axisymmetric model.

Finally, we must note that the tropical cyclone in the present model developed in a closed domain. A three-dimensional tropical cyclone model constructed by Kurihara and Tuleya (1974) is also bounded by lateral walls. In future numerical modeling, a tropical cyclone should be treated not as an isolated system but in the context of the general circulation of the atmosphere. This naturally requires the use of an improved three-dimensional simulation model.

REFERENCES

Anthes, R. A., 1972: Development of asymmetries in a three-dimensional numerical model of the tropical cyclone. *Mon. Wea. Rev.*, **100**, 461–476.

——, S. L. Rosenthal and J. W. Trout, 1971a: Preliminary results from an asymmetric model of the tropical cyclone. *Mon. Wea. Rev.*, **99**, 744–758.

——, J. W. Trout and S. L. Rosenthal, 1971b: Comparisons of tropical cyclone simulations with and without the assumption of circular symmetry. *Mon. Wea. Rev.*, **99**, 759–766.

Delsol, F., K. Miyakoda and R. H. Clarke, 1971: Parameterized processes in the surface boundary layer of an atmospheric circulation model. *Quart. J. Roy. Meteor. Soc.*, **97**, 181–208.

Ellison, T. H., 1957: Turbulent transport of heat and momentum from an infinite rough plane. *J. Fluid Mech.*, **2**, 456–466.

Gray, W. M., 1967: The mutual variation of wind, shear, and baroclinicity in the cumulus convective atmosphere of the hurricane. *Mon. Wea. Rev.*, **95**, 55–73.

——, and D. J. Shea, 1973: The hurricane's inner core region. II. Thermal stability and dynamic characteristics. *J. Atmos. Sci.*, **30**, 1565–1576.

Hawkins, H. F., and D. T. Rubsam, 1968: Hurricane Hilda, 1964: II. Structure and budgets of the hurricane on October 1, 1964. *Mon. Wea. Rev.*, **96**, 617–636.

Koteswaram, P., 1967: On the structure of hurricanes in the upper troposphere and lower stratosphere. *Mon. Wea. Rev.*, **95**, 541–564.

Kurihara, Y., 1968: Note on finite difference expressions for the hydrostatic relation and pressure gradient force. *Mon. Wea. Rev.*, **96**, 654–656.

——, 1973: A scheme of moist convective adjustment. *Mon. Wea. Rev.*, **101**, 547–553.

——, and R. E. Tuleya, 1974: Structure of a tropical cyclone developed in a three-dimensional numerical simulation model. *J. Atmos. Sci.*, **31**, 893–919.

Malkus, J. S., and H. Riehl, 1960: On the dynamics and energy transformations in steady-state hurricanes. *Tellus*, **12**, 1–20.

McIntyre, M. E., 1970: Diffusive destabilization of the baroclinic circular vortex. *Geophys. Fluid Dyn.*, **1**, 19–57.

Ogura, Y., 1964: Frictionally controlled, thermally driven circulations in a circular vortex with application to tropical cyclones. *J. Atmos. Sci.*, **21**, 610–621.

Ooyama, K., 1966: On the stability of the baroclinic circular vortex: A sufficient criterion for instability. *J. Atmos. Sci.*, **23**, 43–53.

——, 1969a: Numerical simulation of the life cycle of tropical cyclones. *J. Atmos. Sci.*, **26**, 3–40.

——, 1969b: Numerical simulation of tropical cyclones with an axi-symmetric model. *Proc. WMO/IUGG Symposium Numerical Weather Prediction, Tokyo, 26 November–4 December 1968*, Japan Meteor. Agency, 81–88.

Palmén, E., 1948: On the formation and structure of tropical hurricane. *Geophysica*, **3**, 26–38.

——, and C. L. Jordan, 1955: Note on the release of kinetic energy in tropical cyclones. *Tellus*, **7**, 186–188.

——, and H. Riehl, 1957: Budget of angular momentum and energy in tropical cyclones. *J. Meteor.*, **14**, 150–159.

——, and C. W. Newton, 1969: *Atmospheric Circulation Systems. Their Structure and Physical Interpretation.* Academic Press, Chap. 15.

Phillips, N. A., 1957: A coordinate system having some special advantages for numerical forecasting. *J. Meteor.*, **14**, 184–185.

Riehl, H., and J. S. Malkus, 1961: Some aspects of Hurricane Daisy, 1958. *Tellus*, **13**, 181–213.

Rosenthal, S. L., 1969: Preliminary results from numerical experiments with a primitive equation model designed to simulate the development of tropical cyclones. *Proc. WMO/IUGG Symposium Numerical Weather Prediction, Tokyo, 26 November–4 December 1968*, Japan Meteor. Agency, 49–59.

——, 1971: The response of a tropical cyclone model to variations in boundary layer parameters, initial conditions, lateral

boundary conditions, and domain size. *Mon. Wea. Rev.*, **99**, 767–777.

Smagorinsky, J., 1963: General circulation experiments with the primitive equations: I. The basic experiment. *Mon. Wea. Rev.*, **91**, 99–164.

Sundqvist, H., 1970: Numerical simulation of the development of tropical cyclones with a ten-level model. Part 1. *Tellus*, **22**, 359–390.

Tuleya, R. E., and Y. Kurihara, 1975: The energy and angular momentum budgets of the three-dimensional tropical cyclone model. *J. Atmos. Sci.*, **32** (in press).

Yamasaki, M., 1968a: Numerical simulation of tropical cyclone development with the use of primitive equations. *J. Meteor. Soc. Japan*, **46**, 178–201.

——, 1968b: Detailed analysis of a tropical cyclone simulated with a 13-layer model. *Papers Meteor. Geophys.*, **19**, 559–585.

——, 1969: Large-scale disturbances in the conditionally unstable atmosphere in low latitudes. *Papers Meteor. Geophys.*, **20**, 289–336.

Yanai, M., 1961a: A detailed analysis of typhoon formation. *J. Meteor. Soc. Japan*, **39**, 187–214.

——, 1961b: Dynamical aspects of typhoon formation. *J. Meteor. Soc. Japan*, **39**, 282–309.

——, 1964: Formation of tropical cyclones. *Rev. Geophys.*, **2**, 367–414.

——, and T. Tokioka, 1969: Axially symmetric meridional motions in the baroclinic circular vortex: A numerical experiment. *J. Meteor. Soc. Japan*, **47**, 183–197.